

Università degli studi di Padova  
Dipartimento di Fisica e Astronomia

Tesi di Dottorato

# Search for heavy resonances decaying into a $Z$ boson and a vector boson in the $\nu\bar{\nu}$ $q\bar{q}$ final state at CMS

Supervisor: Prof. Franco Simonetto  
Candidate: Lisa Benato

Scuola di Dottorato di Ricerca, XXX ciclo



"I have no special talent. I am only passionately curious."  
(A. Einstein)



# Contents

<b>1</b>	<b>Introduction</b>	<b>1</b>
<b>2</b>	<b>Theoretical motivation</b>	<b>3</b>
2.1	Beyond Standard Model theories . . . . .	3
2.2	Heavy Vector Triplet . . . . .	5
2.2.1	Simplified Lagrangian . . . . .	5
2.2.2	Mass eigenstates, mixing parameters and decay widths . . . . .	6
2.2.3	HVT production . . . . .	10
2.2.4	Benchmark model A: weak coupling scenario . . . . .	11
2.2.5	Benchmark model B: strong coupling scenario . . . . .	12
2.2.6	Search for HVT resonances at LHC . . . . .	13
2.3	Warped extra dimension . . . . .	16
2.3.1	Randall-Sundrum original model (RS1) . . . . .	16
2.3.2	Bulk extension of RS1: graviton production and decays . . . . .	19
2.3.3	Search for KK bulk gravitons at LHC . . . . .	22
<b>3</b>	<b>The Large Hadron Collider and the CMS experiment</b>	<b>25</b>
3.1	The Large Hadron Collider . . . . .	25
3.1.1	Proton-proton interactions . . . . .	28
3.2	CMS detector . . . . .	29
3.2.1	The coordinate system . . . . .	30
3.2.2	The magnet . . . . .	31
3.2.3	The tracking system . . . . .	31
3.2.4	The electromagnetic calorimeter . . . . .	34
3.2.5	The hadronic calorimeter . . . . .	35
3.2.6	The muon system . . . . .	36
3.2.7	The trigger system and data acquisition . . . . .	37
3.2.8	Particle Flow event reconstruction . . . . .	38
3.2.9	Physics objects . . . . .	40
3.3	ATLAS, ALICE, LHCb detectors . . . . .	40
3.3.1	ATLAS . . . . .	40

3.3.2	ALICE . . . . .	41
3.3.3	LHCb . . . . .	41
<b>4</b>	<b>Search for diboson resonances in the <math>ZV \rightarrow \nu\bar{\nu}q\bar{q}</math> final state</b>	<b>43</b>
4.1	Data and Monte Carlo samples . . . . .	44
4.2	Event selection . . . . .	45
4.2.1	Vertex and Pile-up . . . . .	45
4.2.2	Electrons . . . . .	45
4.2.3	Muons . . . . .	46
4.2.4	Taus . . . . .	47
4.2.5	Photons . . . . .	48
4.2.6	Jets . . . . .	49
4.2.7	Jet mass . . . . .	52
4.2.8	Jet substructure . . . . .	53
4.2.9	b-tagging . . . . .	54
4.2.10	Missing Energy . . . . .	54
4.3	Diboson candidate reconstruction . . . . .	56
4.4	Background estimation . . . . .	57
4.5	Systematic uncertainties . . . . .	58
4.6	Results . . . . .	59
<b>5</b>	<b>Combination of diboson searches in semileptonic final states</b>	<b>61</b>
<b>6</b>	<b>Conclusions</b>	<b>63</b>

## CONTENTS

---

1

# Abstract

2

3

## **CONTENTS**

---

---

# Introduction

7 This analysis searches for signal of heavy resonances decaying into a pair of heavy vector  
8 bosons. One Z boson is identified through its invisible decay ( $\nu\nu$ ), while the other is required  
9 to decay hadronically into a pair of quarks. The final states probed by this analysis therefore  
10 consists in two quarks and two neutrinos, reconstructed as missing transverse energy (met).  
11 The hadronically decaying boson (Z, W) is reconstructed as a fat jet, whose mass is used to  
12 define the signal region. Two purity categories are exploited, based on the n-subjettiness of the  
13 fat jet.

14 The search is performed by examining the distribution of the diboson reconstructed trans-  
15 verse mass of the resonance VZ (mtVZ) for a localized excess. The shape and normalization  
16 of the main background of the analysis (V+jets) are estimated with an hybrid approach using  
17 the distribution of data in the sidebands, corrected for a function accounting for potential  
18 differences between the signal region and the sidebands, while the minor background sources  
19 are taken from simulations.



# Theoretical motivation

23 The standard model (SM) of particles represents, so far, the best available description of the  
 24 particles and their interactions. It is the summation of two gauge theories: the electroweak  
 25 interaction, that portrays the weak and electromagnetic interactions together, and the strong  
 26 interaction, or Quantum Chromodynamics (QCD). Particles, namely quarks and leptons, are  
 27 described as spin 1/2 fermions, whilst interactions are represented by spin 1 bosons. The  
 28 symmetry group of the standard model is:

$$SU_C(3) \times SU_L(2) \times U_Y(1), \quad (2.1)$$

29 where the first factor is related to strong interactions, whose mediators are eight gluons,  
 30 while  $SU_L(2) \times U_Y(1)$  is the electroweak symmetry group, whose mediators are photons and  
 31  $Z-W^\pm$  bosons.

32 In renormalizable theories, with no anomalies, all gauge bosons are expected to be massless,  
 33 in contrast with our experimental knowledge. This inconsistency is solved by introducing a  
 34 new scalar particle, the Higgs boson, that can give mass to weak bosons and fermions via the  
 35 spontaneous symmetry breaking mechanism.

36 In the last decades, Standard Model has been accurately probed by many experimental  
 37 facilities (LEP, Tevatron, LHC), and the results lead to an impressive agreement between  
 38 theoretical predictions and experiments. The discovery of the Higgs boson at the CERN Large  
 39 Hadron Collider, measured by both CMS and ATLAS collaborations [1–7], represents not only  
 40 an extraordinary confirmation of the model, but also the latest biggest achievement in particle  
 41 physics as a whole.

## 43 2.1 Beyond Standard Model theories

44 Even though the Standard Model is the most complete picture of the universe of the particles,  
 45 many questions are still left open. From a phenomenological point of view, some experimental  
 46 observations are not included in the theory:

- 47 • in SM, neutrinos are massless (whilst experimentally their masses are confirmed to be  
 48 non-zero, i.e. by the neutrino oscillations);

- 49     • no candidates for dark matter are predicted;
- 50     • no one of the fields included in the SM can explain the cosmological inflation;
- 51     • SM can not justify the matter-antimatter asymmetry.
- 52 From a purely theoretical perspective, some issues are still relevant in the formulation of the  
53 model:
- 54     • *Flavour problem.*  
55     The Standard Model has 18 free parameters: 9 fermionic masses; 3 angular parameters in  
56     Cabibbo-Kobayashi-Maskawa matrix, plus 1 phase parameter; electromagnetic coupling  
57      $\alpha$ ; strong coupling  $\alpha_{\text{strong}}$ ; weak coupling  $\alpha_{\text{weak}}$ ; Z mass; the mass of the Higgs boson.  
58     Such a huge number of degrees of freedom marks the SM as weakly predictive in the  
59     flavour sector.
- 60     • *Unification.*  
61     There is not a “complete” unification of strong, weak and electromagnetic interactions,  
62     since each one has its own coupling constant, behaving differently at different energy  
63     scales; not to mention the fact that gravitational interaction is completely excluded from  
64     the SM.
- 65     • *Hierarchy problem.*  
66     From Quantum Field Theory, it is known that perturbative corrections to the mass of  
67     the scalar bosons included in the theory tend to make it increase towards the energy  
68     scale at which the considered theory still holds [8]. If the Standard Model is seen as  
69     a low-mass approximation of a more general theory valid up to the Planck mass scale  
70     (*i.e.*,  $\sim 1.2 \times 10^{19}$  GeV), a fine-tuning cancellation of the order of 1 over  $10^{34}$  is needed  
71     in order to protect the Higgs mass at the electroweak scale ( $\sim 100$  GeV). Such an aston-  
72     ishing correction is perceived as very unnatural.
- 73     Numerous Beyond Standard Model theories (BSM) have been proposed in order to over-  
74     come the limits of the Standard Model.
- 75     Grand Unified Theories (GUT) aim at extending the symmetry group of the SM (eq. 2) into  
76     largest candidates, such as  $S0(10)$ ,  $SU(5)$  and  $E(6)$ . At GUT scale, approximately at  $10^{16}$  GeV,  
77     non-gravitational interactions are expected to be ruled by only one coupling constant,  $\alpha_{\text{GUT}}$ .
- 78     Super Symmetryc (SUSY) models state that every fermion (boson) of the Standard Model has a  
79     bosonic (fermionic) superpartner, with exactly the same quantum numbers, except the spin. If  
80     SUSY is not broken, each couple of partners and superpartners should have the same masses,  
81     hypothesis excluded by the non-observation of the s-electron. Super Symmetry represents a  
82     very elegant solution of the hierarchy problem of the Higgs boson mass, since the perturba-  
83     tive corrections brought by new SUSY particles exactly cancel out the divergences caused by  
84     SM particles corrections. A particular sub-class of SUSY models, Minimal Super Symmetric  
85     Standard Models, is characterized by the introduction of a new symmetry, the R-parity, that  
86     guarantees the proton stability and also the stability of the lightest SUSY particle, a possible  
87     good candidate for dark matter.
- 88
- 89     Two other possible theoretical pictures are extensively described in sec. 2.2-2.3.

## 90 2.2 Heavy Vector Triplet

91 The heavy vector triplet model [9] provides a general framework aimed at studying new  
 92 physics beyond the standard model, that can manifest into the appearance of new resonances.  
 93 The adopted approach is that of the simplified model, in which an effective Lagrangian is  
 94 introduced, in order to describe the properties and interactions of new particles (in this case,  
 95 a triplet of spin-1 bosons) by using a limited set of parameters, that can be easily linked  
 96 to the physical observables at the LHC experiments. These parameters can describe many  
 97 physical motivated theories (such as sequential extensions of the SM [10, 11] or Composite  
 98 Higgs [12, 13]).

99 Since a simplified model is not a complete theory, its validity is restricted to the on-shell  
 100 quantities related to the production and decay mechanisms of the new resonances, that is how  
 101 most of the LHC BSM searches are performed. Given these conditions, experimental results  
 102 in the resonant region are sensitive to a limited number of the phenomenological Lagrangian  
 103 parameters (or to a combination of those), whilst the remaining parameters tend to influence  
 104 the tail of the distributions.

105 Limits on production cross-section times branching ratio ( $\sigma\mathcal{B}$ ), as a function of the invariant  
 106 mass spectrum of the probed resonance, can be extracted from experimental data. Given that  
 107  $\sigma\mathcal{B}$  are functions of the simplified model parameters and of the parton luminosities, it is then  
 108 possible to interpret the observed limits in the parameter space.

### 109 2.2.1 Simplified Lagrangian

110 The heavy vector triplet framework assumes the existence of an additional vector triplet,  $V_\mu^a$ ,  
 111  $a = 1, 2, 3$ , in which two spin-1 particles are charged and one is neutral:

$$V_\mu^\pm = \frac{V_\mu^1 \mp i V_\mu^2}{\sqrt{2}}; \quad (2.2)$$

$$V_\mu^0 = V_\mu^3.$$

112  
 113 The triplet interactions are described by a simplified Lagrangian, that is invariant under SM  
 114 gauge and CP symmetry, and accidentally invariant under the custodial symmetry  $SU(2)_L \times$   
 115  $SU(2)_R$ :

$$\begin{aligned} \mathcal{L}_V = & -\frac{1}{4} \left( D_\mu V_\nu^a - D_\nu V_\mu^a \right) \left( D^\mu V^\nu{}^a - D^\nu V^\mu{}^a \right) + \frac{m_V^2}{2} V_\mu^a V^\mu{}^a \\ & + ig_V c_H V_\mu^a \left( H^\dagger \tau^a D^\mu H - D^\mu H^\dagger \tau^a H \right) + \frac{g^2}{g_V} c_F V_\mu^a \sum_f \bar{f}_L \gamma^\mu \tau^a f_L \\ & + \frac{g_V}{2} c_{VVV} \epsilon_{abc} V_\mu^a V_\nu^b (D^\mu V^\nu{}^c - D^\nu V^\mu{}^c) + g_V^2 c_{VVH} V_\mu^a V^\mu{}^a H^\dagger H - \frac{g}{2} c_{VW} \epsilon_{abc} W^{\mu\nu}{}^a V_\mu^b V_\nu^c. \end{aligned} \quad (2.3)$$

116  
 117 In the first line of the formula 2.3,  $V$  mass and kinematic terms are included, described with  
 118 the covariant derivative  $D_\mu V_\nu^a = \partial_\mu V_\nu^a + g \epsilon^{abc} W_\mu^b V_\nu^c$ , where  $W_\mu^a$  are the fields of the weak inter-  
 119 action and  $g$  is the weak gauge coupling.  $V_\mu^a$  are not mass eigenstates, since they mix with the  
 120 electroweak fields after the spontaneous symmetry breaking, therefore  $m_V$  isn't the physical

121 mass of the  $V$  bosons.  
 122 The second line describes the interaction of the triplet with the Higgs field and the SM left-  
 123 handed fermions;  $c_H$  describes the vertices with the physical Higgs and the three unphysical  
 124 Goldstone bosons that, for the Goldstone equivalence theorem, are equivalent to the longitu-  
 125 dinal polarization of  $W$  and  $Z$  bosons at high-energy; hence,  $c_H$  is related to the bosonic decays  
 126 of the resonances.  $c_F$  is the analogous parameter describing the  $V$  interaction with fermions,  
 127 that can be generalized as a flavour dependent coefficient, once defined  $J_F^{\mu a} = \sum_f \bar{f}_L \gamma^\mu \tau^a f_L$ :  
 128  $c_F V_\mu^a J_F^{\mu a} = c_\ell V_\mu^a J_\ell^{\mu a} + c_q V_\mu^a J_q^{\mu a} + c_3 V_\mu^a J_3^{\mu a}$ .  
 129 The last part of the equation includes terms that are relevant only in strongly coupled scenar-  
 130 ios (see sec. 2.2.2.2) through the  $V$ - $W$  mixing, but it does not include vertices of  $V$  with light  
 131 SM fields, hence it can be neglected while describing the majority of the LHC phenomenol-  
 132 ogy, under the assumptions previously stated. Additional dimension four quadrilinear  $V$   
 133 interactions are non relevant for the processes discussed, otherwise their effects would be ap-  
 134 preciated in electroweak precision tests and precise Higgs coupling measurements [14].  
 135

136 The parameters in the Lagrangian can be interpreted as follows:  $g_V$  describes the strength  
 137 of the interaction, that is weighted by  $c$  parameters.  $g_V$  ranges from  $g_V \sim 1$  when the coupling  
 138 is weak (sec. 2.2.4), to  $g_V \sim 4\pi$  when the coupling is strong (sec. 2.2.5).  $c$  parameters are  
 139 expected to be  $c \sim 1$ , except to  $c_H$ , that can be smaller for weak couplings. The combinations  
 140 describing the vertices,  $g_V c_H$  and  $g^2/g_V c_F$ , can be considered as the fundamental parameters,  
 141 used to interpret the experimental results.

## 142 2.2.2 Mass eigenstates, mixing parameters and decay widths

143 The newly introduced  $SU(2)_L$  triplet is expected to mix with the weak SM fields. The  $U(1)_{em}$   
 144 symmetry is left unbroken by the new interaction, hence the massless combination of the  
 145 electroweak fields, namely the photon, is the same as the SM:

$$A_\mu = B_\mu \cos \theta_W + W_\mu^3 \sin \theta_W, \quad (2.4)$$

146 with the usual definitions of the electroweak parameters:

$$\begin{aligned} \tan \theta_W &= \frac{g'}{g} \\ e &= \frac{gg'}{\sqrt{g^2 + g'^2}} \\ g &= e / \sin \theta_w \\ g' &= e / \cos \theta_w. \end{aligned} \quad (2.5)$$

147 The  $Z$  boson, on the other hand, mixes with the neutral component of the triplet,  $V^0$ , with  
 148 a rotation parametrized with the angle  $\theta_N$ :

$$\begin{pmatrix} \cos \theta_N & \sin \theta_N \\ -\sin \theta_N & \cos \theta_N \end{pmatrix} \begin{pmatrix} Z \\ V^0 \end{pmatrix}. \quad (2.6)$$

149 The mass matrix of the rotated system is given by:

$$\mathbb{M}_N^2 = \begin{pmatrix} \hat{m}_Z^2 & c_H \zeta \hat{m}_Z \hat{m}_V \\ c_H \zeta \hat{m}_Z \hat{m}_V & \hat{m}_V^2 \end{pmatrix}, \quad (2.7)$$

## 2.2 Heavy Vector Triplet

---

150 where the parameters are defined as:

$$\begin{cases} \hat{m}_Z = \frac{e}{2 \sin \theta_W \cos \theta_W} \hat{v} \\ \hat{m}_V^2 = m_V^2 + g_V^2 c_{VVHH} \hat{v}^2 \\ \zeta = \frac{g_V \hat{v}}{2 \hat{m}_V} \\ \frac{\hat{v}^2}{2} = \langle H^\dagger H \rangle \end{cases}, \quad (2.8)$$

151 and  $\hat{v}$ , the vacuum expectation value of the Higgs field, can be different from the SM  $v = 246$   
152 GeV. The physical masses of  $Z$  and  $V^0$ ,  $m_Z$  and  $M_0$ , and  $\theta_N$  come from the matrix relations:

$$\begin{aligned} \text{Tr}(\mathbb{M}_N^2) &= \hat{m}_Z^2 + \hat{m}_V^2 = m_Z^2 + M_0^2 \\ \|\mathbb{M}_N^2\| &= \hat{m}_Z^2 + \hat{m}_V^2 (1 - c_H^2 \zeta^2) = m_Z^2 M_0^2 \\ \tan 2\theta_N &= \frac{2c_H \zeta \hat{m}_Z \hat{m}_V}{\hat{m}_V^2 - \hat{m}_Z^2}. \end{aligned} \quad (2.9)$$

153 The  $W^\pm$  bosons mix with the charged components of the triplet,  $V^\pm$ , leading to a mass  
154 matrix analogous to eq. 2.10:

$$\mathbb{M}_C^2 = \begin{pmatrix} \hat{m}_W^2 & c_H \zeta \hat{m}_W \hat{m}_V \\ c_H \zeta \hat{m}_W \hat{m}_V & \hat{m}_V^2 \end{pmatrix}, \quad (2.10)$$

155 where  $\hat{m}_W$  is defined as:

$$\begin{cases} \hat{m}_W = \frac{e}{2 \sin \theta_W} \hat{v} = \hat{m}_Z \cos \theta_W \end{cases}; \quad (2.11)$$

156 the physical masses of  $W$  and  $V^\pm$ ,  $m_W$  and  $M_\pm$ , and the angle  $\theta_C$  parametrizing the rotation  
157 of the charged sector are described by:

$$\begin{aligned} \text{Tr}(\mathbb{M}_C^2) &= \hat{m}_W^2 + \hat{m}_V^2 = m_W^2 + M_\pm^2 \\ \|\mathbb{M}_C^2\| &= \hat{m}_W^2 + \hat{m}_V^2 (1 - c_H^2 \zeta^2) = m_W^2 M_\pm^2 \\ \tan 2\theta_C &= \frac{2c_H \zeta \hat{m}_W \hat{m}_V}{\hat{m}_V^2 - \hat{m}_W^2}. \end{aligned} \quad (2.12)$$

158 The custodial symmetry of eq. 2.3 guarantees that:

$$\mathbb{M}_C^2 = \begin{pmatrix} \cos \theta_W & 0 \\ 0 & 1 \end{pmatrix} \mathbb{M}_N^2 \begin{pmatrix} \cos \theta_W & 0 \\ 0 & 1 \end{pmatrix}. \quad (2.13)$$

159

160 By taking the determinant of these matrices, a custodial relation among the masses can be  
161 extracted:

$$m_W^2 M_\pm^2 = \cos \theta_W m_Z^2 M_0^2, \quad (2.14)$$

162 that has some very important consequences.

163 Given that this model aims at searching new particles in the TeV scale and that the scale of  
164 the electroweak interactions must lay at  $\sim 100$  GeV, a hierarchy of the physical masses seems  
165 very natural:

$$\frac{\hat{m}_{(W,Z)}}{\hat{m}_V} \sim \frac{m_{(W,Z)}}{M_{(\pm,0)}} \ll 1; \quad (2.15)$$

<sup>166</sup>  $\zeta$  parameter can be  $\zeta \ll 1$  (weakly coupled scenario) or  $\zeta \sim 1$  (strongly coupled scenario).  
<sup>167</sup> When eq. 2.15 applies, the second lines in eq. 2.9 and eq. 2.12 can be approximated as follows:

<sup>168</sup>

$$\begin{aligned} m_Z^2 &= \hat{m}_Z^2 (1 - c_H^2 \zeta^2) (1 + \mathcal{O}(\hat{m}_Z^2 / \hat{m}_V^2)) \\ m_W^2 &= \hat{m}_W^2 (1 - c_H^2 \zeta^2) (1 + \mathcal{O}(\hat{m}_W^2 / \hat{m}_V^2)). \end{aligned} \quad (2.16)$$

<sup>169</sup>

<sup>170</sup> From eq. 2.11, the ratio of the physical masses of the charged and neutral electroweak bosons  
<sup>171</sup> can be approximated as:

$$\frac{m_W^2}{m_Z^2} \approx \cos \theta_W^2, \quad (2.17)$$

<sup>172</sup> that satisfies the SM tree-level relation  $\rho = 1$  if  $\cos \theta_W^2 \approx 1 - 0.23$ . Adding this approximation  
<sup>173</sup> into eq. 2.14, the  $V$  bosons are expected to have the same masses, hence the same production  
<sup>174</sup> rates:

$$M_{\pm}^2 = M_0^2 (1 + \mathcal{O}(%)). \quad (2.18)$$

<sup>175</sup> The degenerate mass of the triplet will be called  $M_V \approx M_{\pm} \approx M_0$ ; given 2.15,  $M_V = \hat{m}_V$ .  
<sup>176</sup> Another consequence of the mass hierarchy (2.15) is that the mixing angles  $\theta_{(N,C)}$  between the  
<sup>177</sup> electroweak fields and the triplet are small:

$$\theta_{(N,C)} \approx c_H \zeta \frac{\hat{m}_{(W,Z)}}{\hat{m}_V} \ll 1, \quad (2.19)$$

<sup>178</sup> hence the couplings among SM particles are very close to the couplings predicted by the SM.

### <sup>179</sup> 2.2.2.1 Decay widths into fermions

<sup>180</sup> The couplings among the triplet and SM fermions are expressed as a function of the rotation  
<sup>181</sup> angles  $\theta_{(C,N)}$  and SM couplings (omitting the CKM matrix elements for quarks):

$$\begin{cases} g_L^N = \frac{g^2}{g_V^2} \frac{c_F}{2} \cos \theta_N + (g_L^Z)_{SM} \sin \theta_N \approx \frac{g^2}{g_V^2} \frac{c_F}{2}, \\ g_R^N = (g_R^Z)_{SM} \sin \theta_N \approx 0 \\ g_L^C = \frac{g^2}{g_V^2} \frac{c_F}{2} \cos \theta_C + (g_L^W)_{SM} \sin \theta_N \approx \frac{g^2}{g_V^2} \frac{c_F}{2}, \\ g_R^C = 0 \end{cases}, \quad (2.20)$$

<sup>182</sup> where  $g_L^W = g/\sqrt{2}$ ;  $g_{L,R}^{W,Z}$  are those predicted by the standard model. The  $V$  bosons interact  
<sup>183</sup> with SM left fermions, and the strength of the couplings with fermions is determined by  
<sup>184</sup>  $g^2/g_V c_F$ , as stated in sec. 2.2.1. The decay width into fermions is then given by:

$$\Gamma_{V^{\pm} \rightarrow f\bar{f}} \approx 2\Gamma_{V^0 \rightarrow f\bar{f}} \approx N_c \left( \frac{g^2 c_F}{g_V} \right)^2 \frac{M_V}{48\pi}, \quad (2.21)$$

<sup>185</sup> where  $N_c$  is the number of colours (3 for quarks, 1 for leptons).

## 2.2 Heavy Vector Triplet

---

### 186 2.2.2.2 Decay widths into bosons

187 As a starting point, a proper choice of the gauge makes the derivation of the approximate  
 188 decay widths easier. While the unitary gauge is very convenient in discussing the electroweak  
 189 symmetry breaking mechanism, since it provides a basis in which the Goldstone components  
 190 of the scalar fields of the theory are set to zero, it does not properly describe the longitudinally  
 191 polarized bosons in high-energy regimes, since it introduces a dependence of the type  $E/m$  in  
 192 the longitudinal polarization vector, not corresponding to the experimental results. This patho-  
 193 logical behaviour can be overcome profiting of the equivalence theorem: while calculating  
 194 the scattering amplitude of an high-energy process, the longitudinally polarized vectors are  
 195 equivalent to their corresponding Goldstone scalars. The scattering amplitude can therefore  
 196 be calculated with Goldstone diagrams.

197 In the so-called equivalent gauge [15], the Higgs doublet is then parametrized as:

$$H = \begin{pmatrix} i\pi_+ \\ \frac{h+h-i\pi_0}{\sqrt{2}} \end{pmatrix}, \quad (2.22)$$

198 and the Goldstones  $\pi_0$  and  $\pi_+$  describe respectively  $W$  and  $Z$  longitudinal bosons;  $h$  is the  
 199 physical Higgs boson. Rewriting the simplified Lagrangian 2.3 with 2.22 parametrization,  
 200 two terms hold the information of the interaction of the  $V$ s with the Goldstones:

$$\mathcal{L}_\pi = \dots + c_H \zeta \hat{m}_V V_\mu^a \partial^\mu \pi^a + \frac{g_V c_H}{2} V_\mu^a \left( \partial^\mu h \pi^a - h \partial^\mu \pi^a + \epsilon^{abc} \pi^b \partial^\mu \pi^c \right) + \dots, \quad (2.23)$$

201 that are ruled by the  $c_H g_V$  parameters combination. When  $\zeta$  parameter is  $\zeta \approx 1$ , the first term  
 202 in eq. 2.23 becomes important, and it is absorbed by a redefinition of the  $V_\mu^a$  and  $\pi^a$  fields,

$$\begin{aligned} V_\mu^a &\rightarrow V_\mu^a + \frac{c_H \zeta}{\hat{m}_V} \partial_\mu \pi^a \\ \pi^a &\rightarrow \frac{1}{\sqrt{1 - c_H^2 \zeta^2}} \pi^a; \quad c_H^2 \zeta^2 < 1. \end{aligned} \quad (2.24)$$

203 By properly taking into account all the terms of the simplified lagrangian in the equivalent  
 204 gauge, the partial widths of the dibosonic decays are ( $\hat{m}_V = M_V$ ):

$$\begin{aligned} \Gamma_{V^0 \rightarrow W_L^+ W_L^-} &\approx \Gamma_{V^\pm \rightarrow W_L^\pm Z_L} \approx \frac{g_V^2 c_H^2 M_V}{192\pi} \frac{(1 + c_H c_{VVV} \zeta^2)^2}{(1 - c_H^2 \zeta^2)^2} = \frac{g_V^2 c_H^2 M_V}{192\pi} (1 + \mathcal{O}(\zeta^2)) \\ \Gamma_{V^0 \rightarrow Z_L h} &\approx \Gamma_{V^\pm \rightarrow W_L^\pm h} \approx \frac{g_V^2 c_H^2 M_V}{192\pi} \frac{(1 - 4c_H c_{VVV} \zeta^2)^2}{(1 - c_H^2 \zeta^2)^2} = \frac{g_V^2 c_H^2 M_V}{192\pi} (1 + \mathcal{O}(\zeta^2)). \end{aligned} \quad (2.25)$$

### 205 2.2.2.3 Decays in fermions and bosons: concluding remarks

206 From eq. 2.21-2.25, some important conclusions can be extracted.

- 207 • When  $\zeta$  parameter is small, all the triplet decays (both in fermions and in dibosons),  
 208 branching fractions and productions are completely determined by  $g^2 c_F / g_V$ ,  $g_V c_H$ , and  
 209 the degenerate mass of the triplet  $M_V$ ,
- 210 •  $c_{VVV}$ ,  $c_{VVHH}$ ,  $c_{VWW}$  can be neglected, as long as the interest is focused in narrow reso-  
 211 nances.

---

### 2.2.3 HVT production

Given the mass scale of the resonances, the production mechanisms expected to be relevant are Drell-Yan (fig. 2.1) and Vector Boson Fusion (VBF) (fig. 2.2).

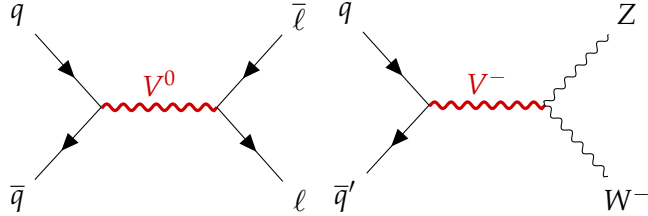


Figure 2.1: Examples of Drell-Yan production mechanism of a heavy  $V$  HVT boson:  $q - \bar{q}$  quark scattering producing a neutral  $V^0$  that decays leptonically (left);  $q - \bar{q}'$  scattering producing a charged  $V^-$  that decays in a  $W$  and  $Z$  bosons (right).

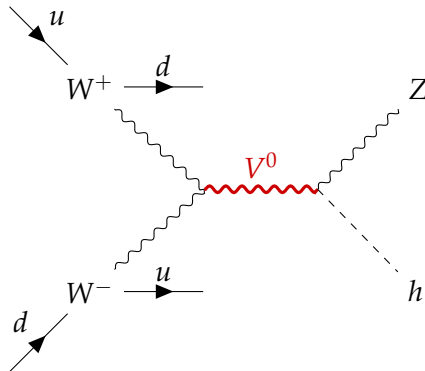


Figure 2.2: Example of VBF production mechanism of a heavy  $V$  HVT boson: a neutral  $V^0$  boson is produced by a couple of  $W$  bosons, as a result of electroweak interactions of initial state  $u$  and  $d$  quarks.  $V^0$  decays in a  $Z$  boson and a Higgs boson. The final state signature includes the presence of a pair of quarks, due to the primary interactions.

The cross-section of the production mechanisms is given by:

$$\sigma(pp \rightarrow V + X) = \sum_{i,j \in p} \frac{\Gamma_{V \rightarrow ij}}{M_V} f(J, S_i, S_j) g(C_i, C_j) \left. \frac{dL_{ij}}{ds} \right|_{s=M_V^2}, \quad (2.26)$$

where  $i, j$  are the partons involved in the hard interaction,  $\Gamma_{ij}$  is the partial width of the process  $V \rightarrow ij$ ,  $f(J, S_i, S_j)$  is a function of the spin of the resonance and of the partons,  $g(C_i, C_j)$  is a function of the colour factors of each parton,  $s$  is the center-of-mass energy and  $\frac{dL_{ij}}{ds}$  are the parton luminosities, that are independent from HVT model (that enters only in  $\Gamma_{ij}$ ).

Parton luminosities, calculated for a center-of-mass energy of 14 TeV starting from quark and antiquark parton distribution functions (PDF), are displayed in fig. 2.3 (Drell-Yan mechanism) and 2.4 (VBF mechanism). VBF luminosities are suppressed by the  $\alpha_{EW}$  factor, therefore the process is relevant only when the bosonic decays of the triplet are dominant (strongly coupled scenario).

## 2.2 Heavy Vector Triplet

---

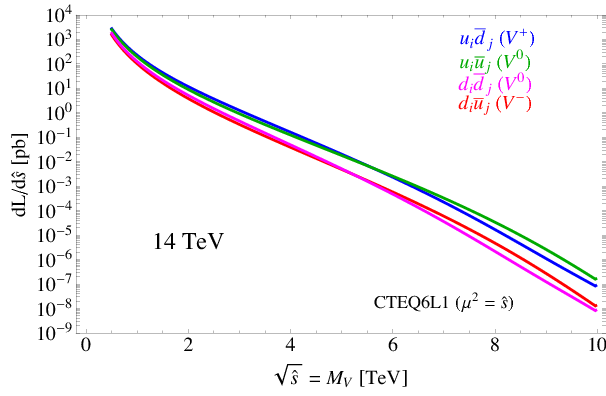


Figure 2.3: Parton luminosities for Drell-Yan process between  $i$  and  $j$  partons, as a function of the parton center-of-mass energy, for the LHC proton-proton collisions performed at 14 TeV.

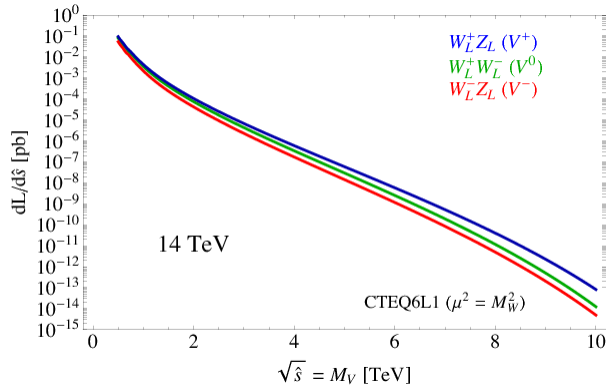


Figure 2.4: Parton luminosities for VBF process between  $i$  and  $j$  partons, as a function of the parton center-of-mass energy, for the LHC proton-proton collisions performed at 14 TeV.

225 **2.2.4 Benchmark model A: weak coupling scenario**

226 Model A scenario aims at reproducing a simple generalization of the SM [10], obtained by ex-  
227 tending the gauge symmetry group with an additional  $SU(2)'$ . The low-energy phenomena  
228 are expected to be dominated by the SM, while the high-energy processes are relevant for the  
229 additional symmetry, bringing additional light vector bosons in play.  
230 It can be shown that this kind of picture is portrayed by HVT when  $c_H \sim -g^2/g_V^2$  and  $c_F \sim 1$ .  
231 This implies that:

$$\begin{aligned} g_V c_H &\approx g^2/g_V \\ g^2 c_F/g_V &\approx g^2/g_V, \end{aligned} \tag{2.27}$$

232 hence the partial decay widths into fermions (eq. 2.21) and bosons (eq. 2.25) differ only by a  
233 factor 2 and the colour factor ( $N_c$ ). Branching fractions for the model A benchmark scenario  
234 ( $g_V = 1$ ) are shown in fig. 2.5 (left); total widths are reported in fig. 2.5 (right) for different  
235 coupling parameters  $g_V$ .

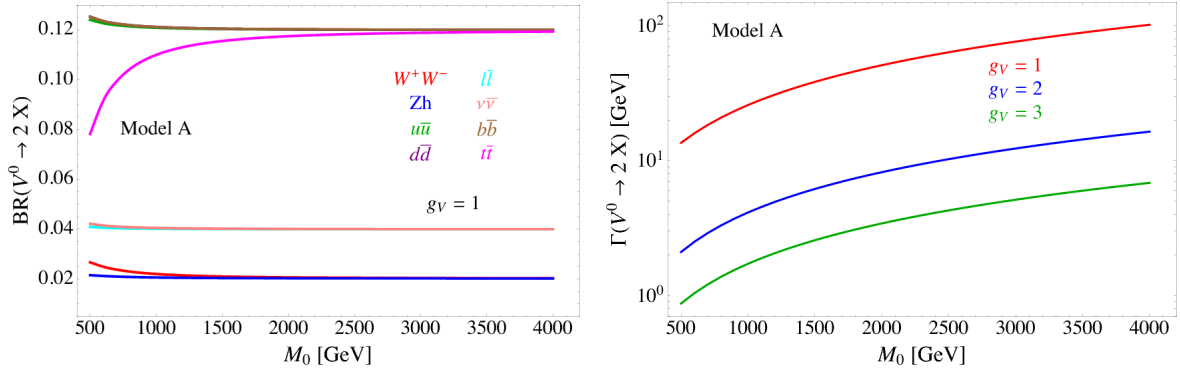


Figure 2.5: HVT model A scenario: branching fractions for fermionic and bosonic decays when  $g_V = 1$  (left) as a function of the mass of the resonance  $M_0$ ; total width of the resonance, as a function of its mass, considering different values of the parameter  $g_V$  (right).

### 2.2.5 Benchmark model B: strong coupling scenario

In composite Higgs models [12], the Higgs boson is the result of the spontaneous symmetry breaking of an  $SO(5)$  symmetry to a  $SO(4)$  group. New vector bosons are expected to appear, and the lightest ones can be represented by HVT model B when  $c_H \sim c_F \sim 1$ .

In this case:

$$\begin{aligned} g_V c_H &\approx -g_V \\ g^2 c_F / g_V &\approx g^2 / g_V, \end{aligned} \quad (2.28)$$

hence the decay into bosons is not suppressed by  $g_V$  parameter. In the benchmark scenario  $g_V = 3$ , decays into dibosons are largely dominant, as it can be seen in fig. 2.6 (left); the total decay width increases for larger  $g_V$  (fig. 2.6, right). When the resonances start to be very broad, *i.e.*  $\Gamma / M_V \gg 0.1$ , the assumptions leading to the simplified model are no longer valid, hence higher order, non-resonant effects must be taken into account.

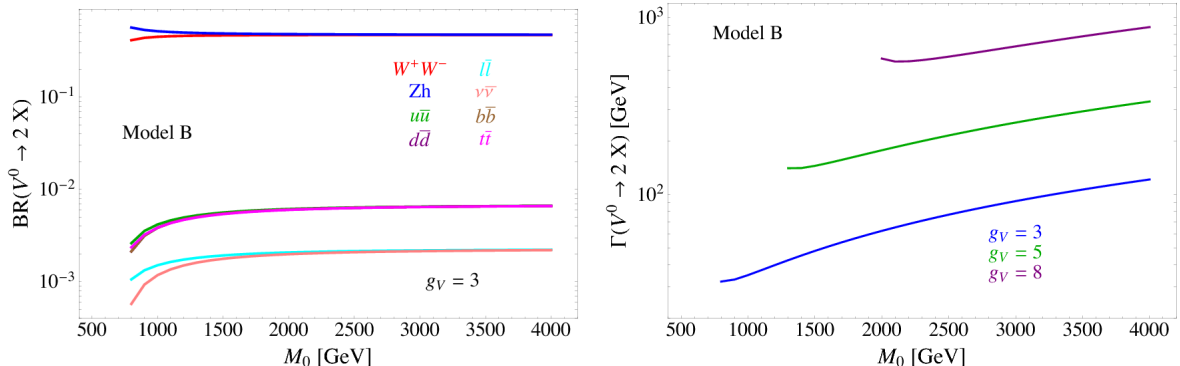


Figure 2.6: HVT model B scenario: branching fractions for fermionic and bosonic decays when  $g_V = 3$  (left) as a function of the mass of the resonance  $M_0$ ; total width of the resonance, as a function of its mass, considering different values of the parameter  $g_V$  (right).

## 2.2 Heavy Vector Triplet

---

### 2.2.6 Search for HVT resonances at LHC

No evidence of HVT resonances has been observed so far at LHC experiments. Data collected by ATLAS and CMS detectors are used to set limits on the HVT resonance masses and coupling parameters. Experimental results from proton-proton collisions performed at a center-of-mass energy of 8 TeV (Run 1 era) at LHC brought to the following conclusions. A weakly coupled resonance, in the context of benchmark model A ( $g_V = 1$ ) was excluded up to 3 TeV by Run 1 data. By looking at parton luminosities in fig.2.3, in data produced by LHC proton-proton collision at 14 TeV, collected for an integrated luminosity of  $300 \text{ fb}^{-1}$ , the sensitivity is expected to increase up to  $m_V \approx 6 \text{ TeV}$ . A strongly coupled resonance, in the context of benchmark model B ( $g_V = 3$ ) is excluded up to 2 TeV by Run 1 data. Data produced by LHC at 14 TeV should increase the sensitivity up to  $m_V \approx 3 - 4 \text{ TeV}$ . The most stringent limits are provided by the latest data produced by LHC at a center-of-mass energy of 13 TeV (Run 2 era).

Numerous searches for HVT triplet have been performed at CMS experiment in different final states: the most sensitive ones were those in all-hadronic topology. [16, 17] (search for  $WW$ ,  $WZ$ ,  $ZZ$  resonances in the  $q\bar{q}q\bar{q}$  final state) excludes a  $W'$  with mass below 3.6 and a  $Z'$  with mass below 2.7 TeV in the model B scenario (fig. 2.7). [18, 19] (search for  $WH$ ,  $ZH$  resonances in the  $q\bar{q}b\bar{b}$  final state) excludes a  $W'$  lighter than 2.97 (3.15) TeV in the HVT model A (model B), and a  $Z'$  up to 1.67 (2.26) TeV in HVT model A (model B) (fig. 2.8). In fig. 2.9, results of [16, 17] (left) and [18, 19] (right) searches are interpreted as exclusion contours in the coupling parameter plane of the HVT model ( $g_V c_H$  and  $g^2 c_F / g_V$ ). In the grey shaded area, the narrow width approximation fails. The colored curves display the parameter exclusion for different mass hypotheses of the triplet. Colored dots show the model A and B benchmark scenarios.

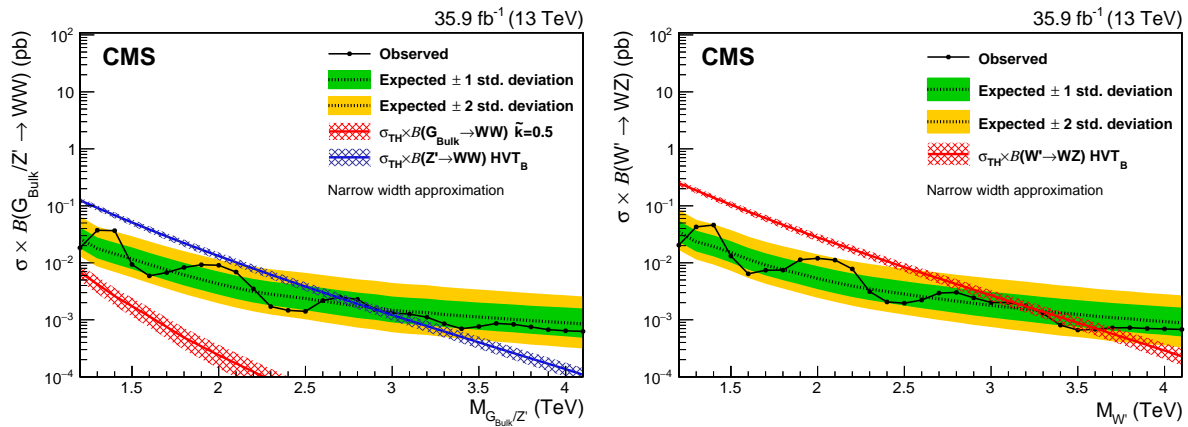


Figure 2.7: The observed and expected limits, with 68% and 95% uncertainty bands, on the product of the cross section and branching fraction  $\sigma \mathcal{B}(Z' \rightarrow WW)$  for a spin-1  $Z'$  (left) and  $\sigma \mathcal{B}(W' \rightarrow WZ)$  for a spin-1  $W'$  (right), as a function of the reconstructed mass of the diboson resonance. The colored lines show the theoretical predictions for the HVT model B.

Many other final states have been exploited at CMS:  $ZW, ZZ \rightarrow \ell\bar{\ell}q\bar{q}$  [20];  $WH, ZH \rightarrow (\ell\bar{\ell}, \ell\nu, \nu\bar{\nu})b\bar{b}$  [21];  $WZ, WW \rightarrow \ell\nu q\bar{q}$  [22]. Finally,  $ZW, ZZ \rightarrow \nu\bar{\nu}q\bar{q}$  [23] results will be extensively described in this thesis.

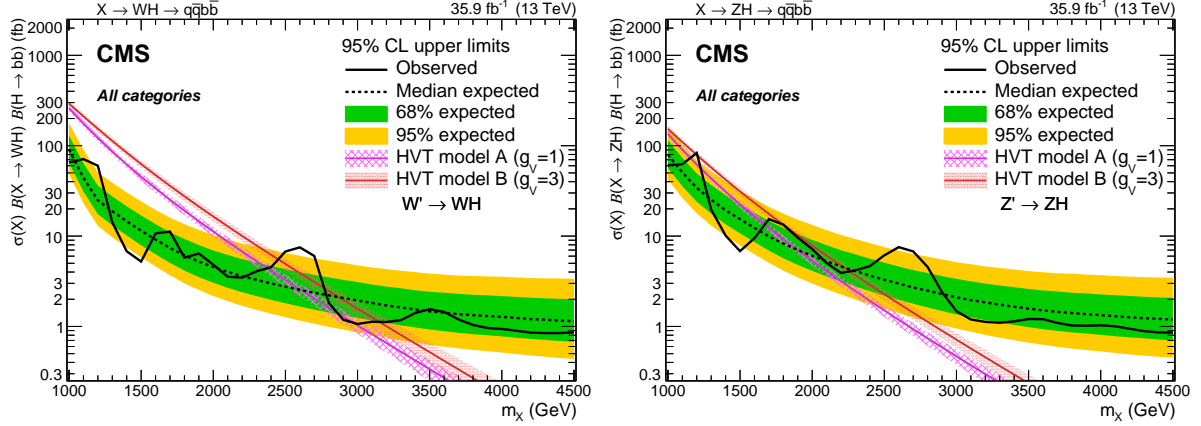


Figure 2.8: The observed and expected limits, with 68% and 95% uncertainty bands, on the product of the cross section and branching fraction  $\sigma\mathcal{B}(W' \rightarrow WH)$  for a spin-1  $W'$  (left) and  $\sigma\mathcal{B}(Z' \rightarrow ZH)$  for a spin-1  $Z'$  (right), as a function of the reconstructed mass of the diboson resonance. The colored lines show the theoretical predictions for the HVT model A and B.

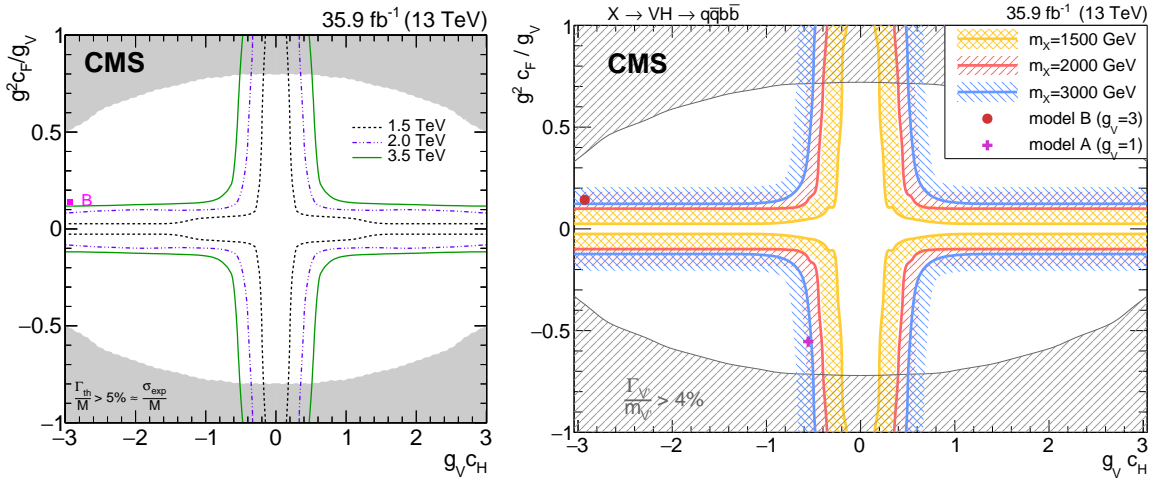


Figure 2.9: Exclusion contours in the coupling parameter plane of the HVT model ( $g_V c_H$  and  $g^2 c_F / g_V$ ).

## 2.2 Heavy Vector Triplet

---

273 Searches for HVT model B resonances have been performed at ATLAS experiment as well.  
 274 Results for a  $W' \rightarrow WZ$  reported in fig. 2.10 include the searches performed in  $WW, WZ, ZZ \rightarrow$   
 275  $q\bar{q}q\bar{q}$  final state [24];  $WZ, WW \rightarrow \ell\nu q\bar{q}$  final state [25];  $ZW, ZZ \rightarrow (\ell\bar{\ell}, \ell\nu, \nu\bar{\nu})q\bar{q}$  final state [26].  
 276 The all-hadronic final state has the best sensitivity and it excludes a  $W'$  resonance up to 3.3  
 277 TeV (model B scenario). Results for a  $W' \rightarrow WH$  and for a  $Z' \rightarrow ZH$  are displayed in fig. 2.11  
 278 (left and right respectively), and they include searches performed in  $WH, ZH \rightarrow q\bar{q}b\bar{b}$  final  
 279 state [27], and  $WH, ZH \rightarrow \ell\bar{\ell}, \ell\nu, \nu\bar{\nu} b\bar{b}$  [28]. A  $W'$  is excluded up to 2.9 TeV and a  $Z'$  is  
 280 excluded up to 2.8 TeV (in the model B scenario).

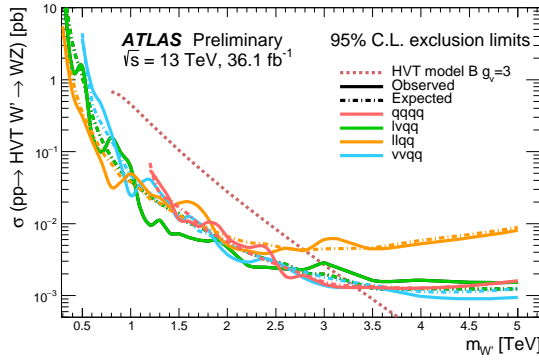


Figure 2.10: The observed and expected limits on the product of the cross section and branching fraction  $\sigma\mathcal{B}(W' \rightarrow WZ)$  for a spin-1  $W'$ , as a function of the reconstructed mass of the diboson resonance. The dotted line shows the theoretical predictions for the HVT model B.

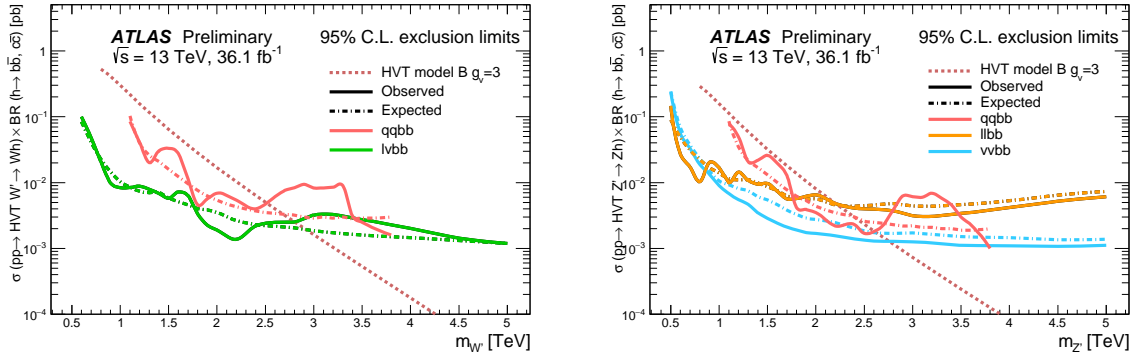


Figure 2.11: The observed and expected limits on the product of the cross section and branching fraction  $\sigma\mathcal{B}(W' \rightarrow WH)$  for a spin-1  $W'$  (left) and  $\sigma\mathcal{B}(Z' \rightarrow ZH)$  for a spin-1  $Z'$  (right), as a function of the reconstructed mass of the diboson resonance. The colored lines show the theoretical predictions for the HVT model B.

<sup>281</sup> **2.3 Warped extra dimension**

<sup>282</sup> The Randall-Sundrum model [29,30] (RS1) proposes the introduction of one additional warped  
 283 dimension in order to solve the hierarchy problem. The metric of the 5-dimensional space (a  
 284 slice of  $AdS_5$ ) generates an exponential hierarchy between the electroweak and Planck scales,  
 285 associated respectively to the TeV three-brane, where the SM particles are confined, and the  
 286 Planck three-brane. As a consequence of the new geometry, spin-2 massive gravitons are pre-  
 287 dicted to exist.

<sup>288</sup> The bulk extension of the Randall-Sundrum model [31,32] states that the SM fields can prop-  
 289 agate in the extra dimension. Light fermions are near the Planck brane, heavy fermions are  
 290 close to the TeV brane, while the Higgs sector is confined in the TeV brane. Higgs couplings  
 291 to the heavy fermions are therefore expected to be stronger: this naturally arising hierarchy  
 292 of the masses of the SM fields gives a solution to the flavour problem. In this scenario, the  
 293 fermionic decays of the bulk gravitons are suppressed, while the bosonic decays are preferred.

<sup>294</sup> **2.3.1 Randall-Sundrum original model (RS1)**

<sup>295</sup> The existence of additional  $n$ -dimensions implies that the effective Planck scale observed in  
 296 4-dimensions,  $M_{PL} = 1.220910^{19}$  GeV, is related to the fundamental  $4+n$ -dimensional Planck  
 297 scale,  $M$ , via the geometry.  $M$  is expected to be of the order of the reduced  $\overline{M}_{PL} = M_{PL}/2\pi$ .  
 298 If the 4-dimensional and the  $n$  additional metrics are factorizable,  $\overline{M}_{PL}$  is the product of  $M$   
 299 and the volume of the compact space  $V_n$ :

$$\overline{M}_{PL}^2 = V_n M^{2+n}. \quad (2.29)$$

<sup>300</sup> If  $M \sim \text{TeV}$ , this implies that  $V_n$  must be very large, hence the compactification scale  $\mu \sim 1/V_n^{1/n}$   
 301 is small (eV – MeV for  $n=2 - 7$ ). Given the smallness of  $\mu$  when compared to the electroweak  
 302 scale, the effects of the extra dimensions should be evident in SM processes. Since they are  
 303 not observed, SM particles are assumed to be confined in a 4-dimensional space, the TeV  
 304 three-brane, while only gravity is allowed to propagate into the  $4+n$ -dimensional space, the  
 305 bulk. This mechanism solves the hierarchy of the Higgs scale but introduces a new hierarchy  
 306 between  $\mu$  and  $M$ .

<sup>307</sup> In the Randall-Sundrum model [29, 30], only one additional dimension is added. The ge-  
 308 ometry of the 5-dimensional bulk is non-factorizable, and it is a slice of  $AdS_5$  spacetime.<sup>1</sup>  
 309 The 4-dimensional metric is multiplied by an exponential function of the fifth dimension (the  
 310 "warp" factor):

$$ds^2 = e^{-2kr_c\phi} \eta_{\mu\nu} dx^\mu dx^\nu + r_c^2 d\phi^2; \quad (2.30)$$

<sup>311</sup>  $x^\mu$  are the usual 4-dimensional coordinates,  $\eta_{\mu\nu} = \text{diag}(-1, 1, 1, 1)$  is the Minkowski metric,  $k$   
 312 is a scale of order of  $\overline{M}_{PL}$ ,  $\phi$  is the coordinate of the extra dimension,  $0 < |\phi| < \pi$ , and  $r_c$  is  
 313 the compactification radius of this finite interval. 4-dimensional mass scales are obtained by  
 314 multiplying the bulk masses by  $e^{-2kr_c\phi}$ : given the exponential form of the warp factor, a small  
 315  $r_c$  suffices for generating a large hierarchy between Planck and Higgs scales.

<sup>316</sup> Two 4-dimensional three-branes are located at the boundaries of the fifth dimension: the  
 317 visible brane at  $\phi = \pi$ ; the hidden brane at  $\phi = 0$ , and their metrics are obtained starting from

---

<sup>1</sup>An  $n$ -dimensional anti-de Sitter space ( $AdS_n$ ) is a maximally symmetric Lorentzian manifold, that solves the Einstein equation with a negative curvature (negative cosmological constant).

## 2.3 Warped extra dimension

---

<sup>318</sup> the bulk 5-dimensional metric  $G_{MN}$ , where  $M, N = \mu, \phi$ :

$$\begin{aligned} g_{\mu\nu}^{\text{vis}}(x^\mu) &= G_{\mu\nu}(x^\mu, \phi = \pi) \\ g_{\mu\nu}^{\text{hid}}(x^\mu) &= G_{\mu\nu}(x^\mu, \phi = 0). \end{aligned} \quad (2.31)$$

<sup>319</sup> The classical action is given by:

$$\begin{aligned} S &= S_{\text{gravity}} + S_{\text{vis}} + S_{\text{hid}} \\ S_{\text{gravity}} &= \int d^4x \int_{-\pi}^{+\pi} d\phi \sqrt{-G} (-\Lambda + 2M^3\mathcal{R}) \\ S_{\text{vis}} &= \int d^4x \sqrt{-g_{\text{vis}}} (\mathcal{L}_{\text{vis}} - V_{\text{vis}}) \\ S_{\text{hid}} &= \int d^4x \sqrt{-g_{\text{hid}}} (\mathcal{L}_{\text{hid}} - V_{\text{hid}}), \end{aligned} \quad (2.32)$$

<sup>320</sup> where  $G$  ( $g$ ) is the trace of the  $G_{MN}$  ( $g_{\mu\nu}$ ) metric,  $\Lambda$  is the cosmological constant in the bulk,  
<sup>321</sup>  $\mathcal{R}$  is the 5-dimensional Ricci scalar,  $\mathcal{L}$  and  $V$  are the lagrangian and the vacuum energy of the  
<sup>322</sup> hidden and visible branes.

<sup>323</sup> A 5-dimensional metric that preserves the 4-dimensional Poincaré invariance has the form:

$$ds^2 = e^{-2\sigma(\phi)} \eta_{\mu\nu} dx^\mu dx^\nu + r_c^2 d\phi^2. \quad (2.33)$$

<sup>324</sup> The Poincaré invariance guarantees that  $r_c$  does not depend on  $x^\mu$ . Given 2.33, the solution of  
<sup>325</sup> the 5-dimensional Einstein's equations simplifies into:

$$\sigma = r_c |\phi| \sqrt{\frac{-\Lambda}{24M^3}}. \quad (2.34)$$

<sup>326</sup> Furthermore, the Poincaré invariance imposes constraints to the vacuum energies and cosmo-  
<sup>327</sup> logical constant:

$$\begin{aligned} V_{\text{hid}} &= -V_{\text{vis}} = 24M^3k \\ \Lambda &= -24M^3k^2. \end{aligned} \quad (2.35)$$

<sup>328</sup> The final 5-dimensional metric is then:

$$ds^2 = e^{-2kr_c|\phi|} \eta_{\mu\nu} dx^\mu dx^\nu + r_c^2 d\phi^2. \quad (2.36)$$

<sup>329</sup> A small  $r_c$  is considered, so the effects of the fifth dimension on 4-dimensional spacetime  
<sup>330</sup> can't be appreciated. A 4-dimensional effective field theory approach is therefore motivated,  
<sup>331</sup> and its mass parameters are related to the bulk parameters,  $M$ ,  $k$  and  $r_c$ . In the Randall-  
<sup>332</sup> Sundrum model, SM matter fields are confined in the TeV brane.

<sup>333</sup> The massless gravitons, the mediators of the gravitational interaction in the effective field  
<sup>334</sup> theory, are the zero modes ( $h_{\mu\nu}$ ) of the quantum fluctuations of the classical solution ( 2.36):

$$ds^2 = e^{-2kT(x)|\phi|} (\eta_{\mu\nu} + h_{\mu\nu}(x)) dx^\mu dx^\nu + T^2(x) d\phi^2, \quad (2.37)$$

<sup>335</sup> where the usual Minkowski metric has been replaced by  $\bar{g}_{\mu\nu}(x) = \eta_{\mu\nu} + h_{\mu\nu}$ ;  $h_{\mu\nu}$  are the  
<sup>336</sup> tensor fluctuations around the Minkowski space, and represent both the physical graviton in  
<sup>337</sup> 4-dimensions and the massless mode of the Kaluza-Klein decomposition of the bulk metric.

<sup>338</sup>  $r_c$  is the vacuum expectation value of  $T(x)$ .

<sup>339</sup> By substituting eq. 2.37 in the classical action 2.32, an effective action can be extracted, and in  
<sup>340</sup> particular the curvature term holds:

$$S_{\text{eff}} \sim \int d^4x \int_{-\pi}^{+\pi} d\phi 2M^3 r_c e^{-2kr_c|\phi|} \bar{\mathcal{R}} \sqrt{-\bar{g}}, \quad (2.38)$$

<sup>341</sup> where  $\bar{g}$  is the trace of  $\bar{g}_{\mu\nu}$  and  $\bar{\mathcal{R}}$  is the 4-dimensional Ricci scalar of  $\bar{g}_{\mu\nu}$  metric. In this  
<sup>342</sup> effective 4-dimensional action, the  $\phi$  dependence can be integrated out, and the 4-dimensional  
<sup>343</sup> Planck mass can be calculated:

$$\bar{M}_{PL}^2 = M^3 r_c \int_{-\pi}^{+\pi} d\phi e^{-2kr_c|\phi|} = \frac{M^3}{k} \left(1 - e^{-2kr_c\pi}\right). \quad (2.39)$$

<sup>344</sup> It can be shown [29] that a field with a fundamental mass parameter  $m_0$  in the bulk manifests  
<sup>345</sup> in the visible three-brane with a physical mass  $m$ :

$$m = e^{-2kr_c\pi} m_0. \quad (2.40)$$

<sup>346</sup> Scales  $m \sim \text{TeV}$  are generated from  $m_0 \sim \bar{M}_{PL}$  if  $e^{kr_c\pi} \sim 10^{15}$ . This relation stands still when  
<sup>347</sup> Higgs field is introduced and confined in the visible three-brane:

$$v = e^{-2kr_c\pi} v_0, \quad (2.41)$$

<sup>348</sup> where  $v$  is the Higgs vacuum expectation value in the TeV brane and  $v_0$  is the 5-dimensional  
<sup>349</sup> Higgs v.e.v.

<sup>350</sup> The hierarchy problem is then solved by the exponential warp factor. The weakness of gravity  
<sup>351</sup> in the TeV three-brane is motivated by the small overlap of the graviton wave function.

<sup>352</sup> In order to calculate the mass spectrum of the graviton in the TeV brane, the tensor fluctuations  
<sup>353</sup> of the Minkowski metric are expanded into a Kaluza-Klein (KK) tower  $h_{\mu\nu}^{(n)}$ :

$$h_{\mu\nu}(x, \phi) = \sum_{n=0}^{\infty} h_{\mu\nu}^{(n)}(x) \frac{\chi^{(n)}(\phi)}{\sqrt{r_c}}. \quad (2.42)$$

<sup>354</sup> Once a suitable gauge is chosen, i.e.  $\eta^{\mu\nu} \partial_\mu h_{\nu\alpha}^{(n)} = \eta^{\mu\nu} h_{\mu\nu}^{(n)} = 0$ , the equation of motion of  $h_{\mu\nu}^{(n)}$   
<sup>355</sup> becomes the Klein-Gordon relation, where  $m_n^G \geq 0$ :

$$\left( \eta^{\mu\nu} \partial_\mu \partial_\nu - (m_n^G)^2 \right) h_{\mu\nu}^{(n)}(x) = 0. \quad (2.43)$$

<sup>356</sup> By substituting eq. 2.42 into Einstein's equation, the solutions for  $\chi^{(n)}(\phi)$  (commonly called  
<sup>357</sup> "profiles") are [33,34]:

$$\chi^{(n)}(\phi) = \frac{e^{2\sigma}}{N} \left[ J_2(z_n^G) + \alpha_n Y_2(z_n^G) \right], \quad (2.44)$$

<sup>358</sup> where  $J_2$  and  $Y_2$  are second order Bessel functions,  $N$  is the normalization of the wavefunction,  
<sup>359</sup>  $\alpha_n$  are coefficients and  $z_n^G = m_n^G e^{\sigma(\phi)}/k$ .  $m_n^G$  is the mass of the  $n$ -mode, and it depends on the  
<sup>360</sup> roots of the Bessel functions  $z_n^G = (3.83, 7.02, 10.17, 13.32, \dots)$ . In the limit  $m_n^G/k \ll 1$  and  
<sup>361</sup>  $e^{kr_c\pi} \gg 1$ :

$$m_n^G = k z_n^G(\pi) e^{-kr_c\pi}. \quad (2.45)$$

## 2.3 Warped extra dimension

---

362 The interactions between the graviton KK modes and the matter fields in the TeV brane can be  
363 derived from the 4-dimensional effective Lagrangian, once  $h_{\mu\nu}$  is replaced by its KK decom-  
364 position:

$$\mathcal{L} = -\frac{1}{M_{PL}} T^{\mu\nu}(x) h_{\mu\nu}^{(0)} - \frac{1}{e^{-kr_c\pi} M_{PL}} T^{\mu\nu}(x) \sum_{n=1}^{\infty} h_{\mu\nu}^{(n)}(x); \quad (2.46)$$

365  $T^{\mu\nu}$  is the space energy-momentum tensor of the matter fields. The zero mode of the gravitons  
366 coupling is  $1/M_{PL}$ , while higher order KK modes couplings to all SM fields are suppressed  
367 by  $e^{-kr_c\pi} M_{PL}$ , that is of the order of the TeV scale. Spin-2 KK masses and couplings are hence  
368 determined by the TeV scale, or, equivalently, KK gravitons are close to the TeV brane. This  
369 implies that KK gravitons can be produced via  $q\bar{q}$  or gluon fusion, and that a leptonic decay  
370 of the resonance could represent a very clear signal signature.

### 371 2.3.2 Bulk extension of RS1: graviton production and decays

372 An extension of the original RS1 formulation has been proposed. It states that the usual SM  
373 fields are no longer confined in the TeV brane, but they are the zero modes of the correspond-  
374 ing 5-dimensional SM fields. If first and second generation fermions are close to the Planck  
375 brane, contribution to flavour changing neutral currents by higher-dimensional operators are  
376 suppressed. These contributions are excluded by electroweak precision tests, but they were  
377 not prevented in original RS1. The second motivation behind the choice is, as mentioned pre-  
378 viously, the naturally arising flavour hierarchy: first and second generation quarks have small  
379 Yukawa couplings to the Higgs sector, confined in the TeV brane, while top quark and bosons  
380 have stronger Yukawa couplings.

381 In this picture, couplings between higher-order KK gravitons and light fermions are strongly  
382 suppressed, resulting into a negligible KK gravitons production via  $q\bar{q}$ , whilst gluon fusion  
383 production becomes dominant. KK gravitons decay into top quarks and Higgs bosons are  
384 dominant, given that both their profiles are near the TeV brane, while leptonic decays are  
385 negligible. Via the equivalence theorem, the Goldstone bosons are equivalent to the longitu-  
386 dinally polarized weak bosons,  $W_L^\pm$  and  $Z_L$ , that have profiles close to the TeV brane. Decays  
387 of KK gravitons into weak dibosons (and production in VBF) are comparable to di-top and  
388 di-Higgs decays.

389

390 The KK decomposition and the KK mass spectrum of the graviton have already been pre-  
391 sented in sec. 2.3.1. The KK decomposition of a massless 5-dimensional gauge field  $A_M(x, \phi)$   
392 is similarly performed [35]:

$$A_\mu(x, \phi) = \sum_{n=0}^{\infty} A_\mu^{(n)}(x) \frac{\chi_A^{(n)}(\phi)}{\sqrt{r_c}}. \quad (2.47)$$

393 The profiles for the gauge fields are:

$$\chi_A^{(n)}(\phi) = \frac{e^\sigma}{N_A} \left[ J_1(z_n^A) + \alpha_n^A Y_1(z_n^A) \right], \quad (2.48)$$

394 where  $J_1$  and  $Y_1$  are first order Bessel functions. Similarly to eq. 2.49, the mass spectrum of  
395 the gauge field is:

$$m_n^A = kz_n^A(\pi) e^{-kr_c\pi}; \quad (2.49)$$

<sup>396</sup> the first roots of the Bessel functions are  $z_n^A = (2.45, 5.57, 8.70, 11.84, \dots)$ .

<sup>397</sup> The Lagrangian expressing the interaction between the  $m$  and  $n$  modes of the bulk field  $F$   
<sup>398</sup> to the  $q$  KK gravitons mode  $G$  is [35]:

$$\mathcal{L}_{G-F} = \sum_{m,n,q} C_{mnq}^{FFG} \frac{1}{M_{PL}} \eta^{\mu\alpha} \eta^{\nu\beta} h_{\alpha\beta}^{(q)}(x) T_{\mu\nu}^{(m,n)}(x), \quad (2.50)$$

<sup>399</sup>  $C_{mnq}^{FFG}$  is the overlap integral of the profiles:

$$C_{mnq}^{FFG} = \int \frac{d\phi}{\sqrt{k}} e^{t\sigma} \chi_F^{(m)} \chi_F^{(n)} \chi_G^{(q)}; \quad (2.51)$$

<sup>400</sup>  $t$  depends on the type of field considered.

<sup>401</sup> The coupling between gluons and the  $q$  KK graviton mode is given by:

$$C_{00q}^{AAG} = e^{k\pi r_c} \frac{2 [1 - J_0(x_n^G)]}{k\pi r_c (x_n^G)^2 |J_2(x_n^G)|}. \quad (2.52)$$

<sup>402</sup> Once eq. 2.52 is put in eq. 2.50, the most significant partial decay widths into the  $q$  KK graviton  
<sup>403</sup> mode are:

$$\begin{aligned} \Gamma(G \rightarrow t_R \bar{t}_R) &\sim N_c \frac{[\tilde{k} x_q^G]^2 m_q^G}{320\pi} \\ \Gamma(G \rightarrow hh) &\sim \frac{[\tilde{k} x_q^G]^2 m_q^G}{960\pi} \\ \Gamma(G \rightarrow W_L^+ W_L^-) &\sim \frac{[\tilde{k} x_q^G]^2 m_q^G}{480\pi} \\ \Gamma(G \rightarrow Z_L Z_L) &\sim \frac{[\tilde{k} x_q^G]^2 m_q^G}{960\pi}, \end{aligned} \quad (2.53)$$

<sup>404</sup> where  $\tilde{k} = k/\overline{M}_{PL}$ ; the total decay width is:

$$\Gamma_G = \frac{13 [\tilde{k} x_q^G]^2 m_q^G}{960\pi}. \quad (2.54)$$

<sup>405</sup> Calculations, so far, have been performed considering  $M \sim \overline{M}_{PL}$  and  $k < M$ , hypotheses  
<sup>406</sup> under which the solution for the bulk metric (eq. 2.36) is valid. Hence,  $\tilde{k} = k/\overline{M}_{PL} \leq 1$  is  
<sup>407</sup> taken as a reference interval. This has also phenomenological consequences on the width of  
<sup>408</sup> the resonance, as stated in eq. 2.54. The total decay width of the lightest KK graviton mode,  
<sup>409</sup> compared to its mass, is shown as a function of  $\tilde{k}$  in fig. 2.12 [36]. At  $\tilde{k} = 1$ , in the bulk  
<sup>410</sup> scenario, the KK graviton width is expected to be few % of its mass, up to 4 TeV (dotted red  
<sup>411</sup> curve). The narrow width approximation holds, hence the resonance properties can be probed  
<sup>412</sup> at the peak, neglecting the effects in the tails of the mass distribution.

<sup>413</sup> The total cross-section of a bulk graviton, produced at LHC in proton-proton interactions  
<sup>414</sup> via gluon fusion (displayed in fig. 2.13), decaying into a couple of vector bosons (for the  
<sup>415</sup> purpose of this thesis, a final state with two longitudinally polarized  $Z$  bosons is considered)

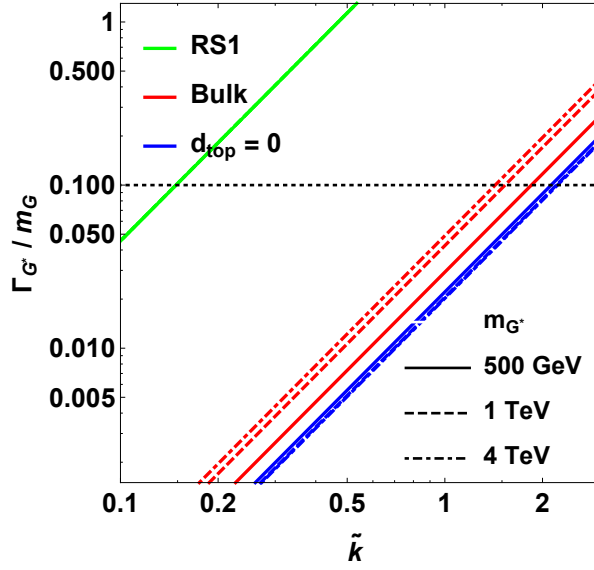


Figure 2.12: Width of the KK gravitons, in units of the mass of the resonance, as a function of the curvature parameter  $\tilde{k}$ . The red curves represent the bulk extension of RS1 original model for different mass hypotheses (from 500 GeV up to 4 TeV).

<sup>416</sup> is expressed as a function of the parton level cross-section  $\hat{\sigma}$ , the gluon parton distribution  
<sup>417</sup> functions  $f_g$ , the momentum transfer  $Q^2 \sim (m_q^G)^2$  and the center-of-mass energy  $s$ :

$$\sigma(pp \rightarrow ZZ) = \int dx_1 dx_2 f_g(x_1, Q^2) f_g(x_2, Q^2) \hat{\sigma}(x_1 x_2 s). \quad (2.55)$$

<sup>418</sup> The differential parton level cross-section, averaged over colors and initial spin states, is (hatted  
<sup>419</sup> quantities are calculated in the center-of-mass frame):

$$\frac{d\hat{\sigma}(gg \rightarrow ZZ)}{d \cos \hat{\theta}} \approx \frac{|\mathcal{M}_{+-00}|^2}{1024\pi \hat{s}}, \quad (2.56)$$

<sup>420</sup> where  $|\mathcal{M}_{+-00}|$  is the matrix element of the dominant contribution in  $gg \rightarrow VV$  process ( $\Gamma_G$   
<sup>421</sup> is defined in eq. 2.54,  $a, b$  are color factors):

$$\mathcal{M}_{+-00}(g^a g^b \rightarrow VV) = -C_{00q}^{AAG} e^{-k\pi r_c} \left( \frac{x_n^G \tilde{k}}{m_n^G} \right)^2 \sum_n \frac{\delta_{ab} \mathcal{A}_{+-00}}{\hat{s} - m_n^G{}^2 + i\Gamma_G m_n^G}. \quad (2.57)$$

<sup>422</sup> The relevant amplitudes taken account in the matrix element calculation are [31]:

$$\mathcal{A}_{+-00} = \mathcal{A}_{-+00} = \frac{(1 - 1/\beta_Z^2) (\beta_Z^2 - 2) [(\hat{t} - \hat{u})^2 - \beta_Z^2 \hat{s}^2] \hat{s}}{8M_Z^2}, \quad (2.58)$$

<sup>423</sup> where  $\beta_Z^2 = 1 - 4M_Z^2/\hat{s}$  and  $M_Z$  is the mass of the  $Z$  boson.

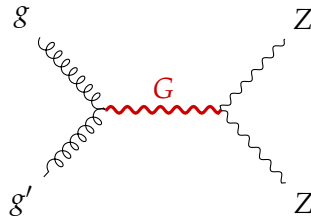


Figure 2.13: Gluon fusion production mechanism for a KK graviton that decays in a couple of  $Z$  bosons.

### 424 2.3.3 Search for KK bulk gravitons at LHC

425 No evidence of spin-2 bulk graviton resonances has been observed so far at LHC experiments.  
 426 Data collected by ATLAS and CMS detectors are used to set limits on the graviton masses,  
 427 generally considering different curvature parameter  $\tilde{k}$  hypotheses, once assured the narrow  
 428 width approximation is still valid (up to  $\tilde{k} \sim 1$ ). The most stringent limits have been set with  
 429 Run 2 data.

430 Many results of the diboson searches performed at CMS and already presented in sec. 2.2.6  
 431 are interpreted in the context of the bulk gravitons, together with the additional final states  
 432  $WZ, ZZ \rightarrow \ell\bar{\nu}\ell\bar{\nu}$  [37] and  $HH \rightarrow b\bar{b}b\bar{b}$  [38]. The most interesting limit is provided by [37], that,  
 433 under the hypothesis  $\tilde{k} = 0.5$ , excludes a spin-2 bulk graviton with a mass lower than 800 GeV  
 434 (fig. 2.14).

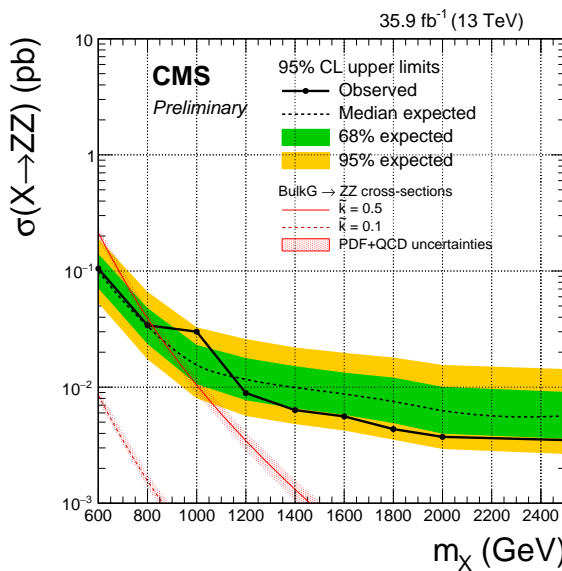


Figure 2.14: The observed and expected limits, with 68% and 95% uncertainty bands, on the product of the cross section and branching fraction  $\sigma\mathcal{B}(G \rightarrow ZZ)$  for a spin-2 bulk graviton, as a function of the reconstructed mass of the diboson resonance. The colored lines show the theoretical predictions for  $\tilde{k} = 0.1$  and  $0.5$ .

435 Similarly for ATLAS experiment, searches for diboson resonances in sec. 2.2.6 have been

## 2.3 Warped extra dimension

---

<sup>436</sup> interpreted in the graviton context. The most stringent limit is given by [25], where, under the  
<sup>437</sup> assumption  $\tilde{k} = 1$ , a spin-2 bulk graviton with mass lower than 1.76 TeV is excluded (fig. 2.15).

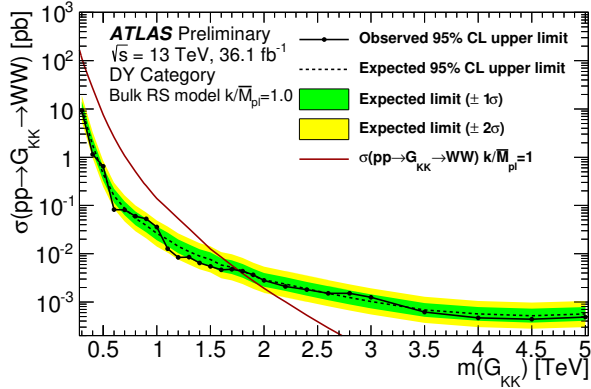


Figure 2.15: The observed and expected limits, with 68% and 95% uncertainty bands, on the product of the cross section and branching fraction  $\sigma\mathcal{B}(G \rightarrow ZZ)$  for a spin-2 bulk graviton, as a function of the reconstructed mass of the diboson resonance. The colored lines show the theoretical predictions for  $\tilde{k} = 1$ .



# The Large Hadron Collider and the CMS experiment

439

440

441 Brief intro to CERN and LHC

442 • research

443 • technology

444 • education

445 • collaboration

446 

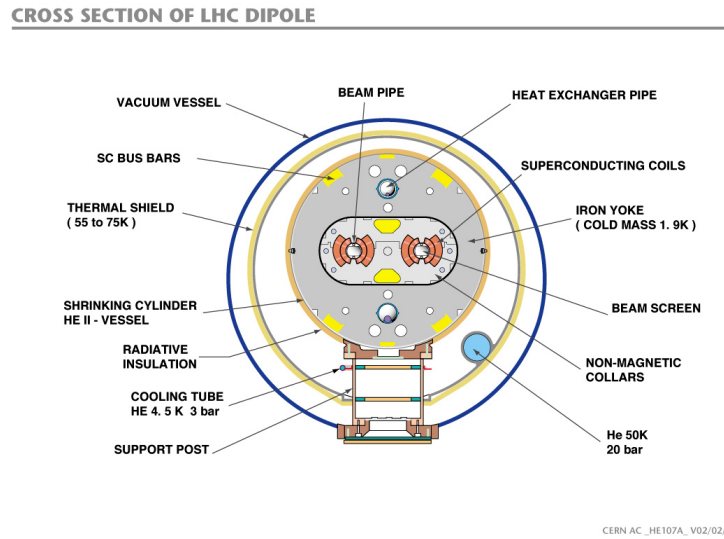
## 3.1 The Large Hadron Collider

447 The Large Hadron Collider (LHC) is a 27 km ring structure designed for the acceleartion  
 448 and collision of protons and heavy ions. It is situated approximatively 100 m underground,  
 449 between France and Switzerland, in the Geneva area, and it is the most important of the  
 450 CERN (Conseil européen pour la recherche nucléaire) facilities. In order to reduce the cost of  
 451 the project, definitively approved in 1996, the LHC has been designed to fit the pre-existing  
 452 underground tunnel of the Large Electron-Positron collider (LEP) [ref. 24 Jacopo], built to  
 453 accelerate electrons and positrons and running until the year 2000.

454 Moving from an electron-positron collider to an hadron collider allowed to reach higher ener-  
 455 gies in the center-of-mass frame, since the synrocotron radiation loss is inversely proportional  
 456 to the fourth power of the mass of the particle involved: hence, it is reduced by a factor  
 457  $m_p/m_e \sim 10^3$ . Furthermore, at a proton-proton collider it is possible to collect higher lumi-  
 458 nosities (and hence more statistics) with regards to, for example, a proton-antiproton collider,  
 459 like Tevatron at Fermilab, in the USA.

460 In the LHC two identical beam pipes rings are designed to let protons circulate in opposite  
 461 directions, in ultrahigh vacuum conditions ( $10^{-11}$ - $10^{-10}$  mbar) in order to avoid collisions  
 462 with gas molecules. Given the reduced available diameter in the tunnel (4 m), the two proton  
 463 beams are magnetically coupled. The collider is composed by 8 arc sections (48 km) driving

464 protons around the ring, and straight sections (6 km) where beam control systems and detec-  
 465 tors are inserted. Proton beams collide in four interaction points, where the four main LHC  
 466 experiments are installed: ALICE, ATLAS, CMS, LHCb.



CERN AC \_HE107A\_ V02/02/98

Figure 3.1: Section of the LHC dipole magnet structure.

467 In fig. 3.1, a slice of the arc section is displayed. Around the beam pipes, two superconducting  
 468 magnetic dipoles are located: they generate vertical magnetic fields in opposite directions.  
 469 The superconducting coils are made of niobium-titanium, materials that are superconducting  
 470 at very low temperature. At the LHC, they are kept at a temperature of 1.9 K (-271.3°C)  
 471 by a closed liquid helium circuit. A current of 11850 A flows through the magnets, without  
 472 any energy loss due to electrical resistance, generating a magnetic field of 8.33 T. Magnets  
 473 of higher order in multipole expansion (quadrupoles, sextupoles, octupoles, ...) are used to  
 474 optimize the proton trajectories; in particular, quadrupoles allow to focus and squeeze the  
 475 beams. Along the LHC ring here are 9593 magnets; 1232 are dipoles, 392 are quadrupoles.  
 476 The LHC represents the final step of the CERN accelerator complex, showed in fig. 3.2. Protons  
 477 are extracted from hydrogen atoms and inserted in the linear accelerator Linac2, that brings  
 478 them to an energy of 50 MeV. They circulate around a little synchrotron, Proton Synchrotron  
 479 Booster, reaching an energy of 1.4 GeV, and then in the Proton Syncrhrotron (PS), where their  
 480 energy is increased to 25 GeV. The second to last step is the Super Proton Synchrtotron, SPS,  
 481 accelerating protons up to 450 GeV. They are finally injected in the Large Hadron Collider,  
 482 where sixteen radiofrequency cavities (RF) accelerate protons inside each beam up to an en-  
 483 ergy of 6.5 TeV, providing a center-of-mass energy of 13 TeV when colliding. The RF cavities  
 484 provide an accelerating electromagnetic field up to 5 MV/m (maximum voltage of 2 MV),  
 485 that oscillates with a frequency of 400 MHz. Like the magnets, the cavities are kept at low  
 486 temperature (4.5 K, or -268.7°C) in order to allow superconducting conditions. The maximum  
 487 beam energy can be reached in 15 minutes. After several hours of collisions (~ 10 hours), the  
 488 quality of the beams deteriorates and they are extracted from the machine and dumped.  
 489  
 490 Protons circulate inside the LHC ring in bunches of  $\sim 10^{11}$  particles each, 80 mm long. Fo-  
 491 cusing magnets allow to reduce the bunch diameter down to 16  $\mu\text{m}$ . Different bunches are  
 492 separated by 25 ns (or,  $\sim 7.5$  m), corresponding to a frequency of 40 MHz and an instant-

### 3.1 The Large Hadron Collider

---

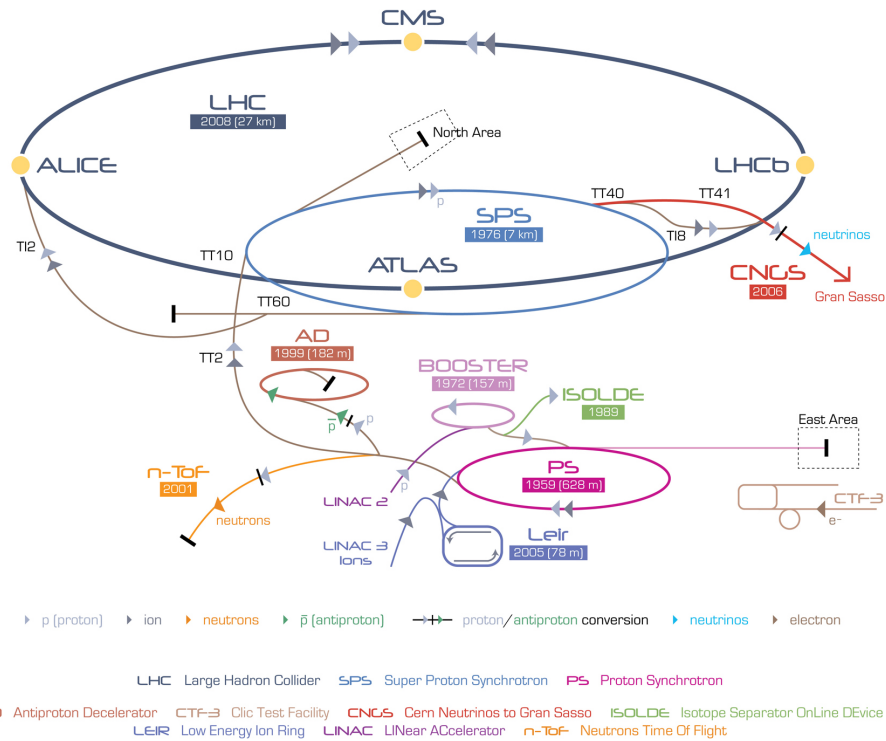


Figure 3.2: The CERN accelerator complex.

neous (peak) luminosity (defined in eq. 3.1) of  $1.2 \times 10^{34} \text{ cm}^{-2}\text{s}^{-1}$ . Given the structure of the beams, at every bunch crossing many protons interact simultaneously: this phenomenon is called pile-up. The designed maximum number of bunches is 2808.

The main parameters that describes an hadronic collider are the center-of-mass energy, corresponding to the sum of the energies of the beams, and the instantaneous luminosity, that describes the frequency of the interactions among the bunches in the beams. If the bunches in the first beam contain  $n_1$  protons, and the bunches in the second beam contain  $n_2$  protons, and if the colliding area is  $\Sigma$ , the frequency of complete turns around the ring is  $f$ , the instantaneous luminosity  $\mathcal{L}_{\text{inst}}$  is:

$$\mathcal{L}_{\text{inst}} = f \frac{n_1 n_2}{\Sigma}. \quad (3.1)$$

If a generic physics process  $i$  has a cross-section of  $\sigma_i$ , the interaction rate  $R_i$  is:

$$R_i = \frac{dN_i}{dt} = \sigma_i \mathcal{L}_{\text{inst}}, \quad (3.2)$$

and the number of events recorded in the time interval  $(0, \tau)$  is obtained by the integrated luminosity  $\mathcal{L} = \int_0^\tau \mathcal{L}_{\text{inst}} dt$ :

$$N_i = \sigma_i \int_0^\tau \mathcal{L}_{\text{inst}} dt. \quad (3.3)$$

In fig. 3.3, a summary of the luminosity measurement in 2016 data is presented. The luminosity delivered by LHC is represented in blue, the recorded by CMS is in orange. The mean number of interaction per bunch crossing (pile-up) is presented as well. The average number of interactions per collision is 27, the maximum is around 50.

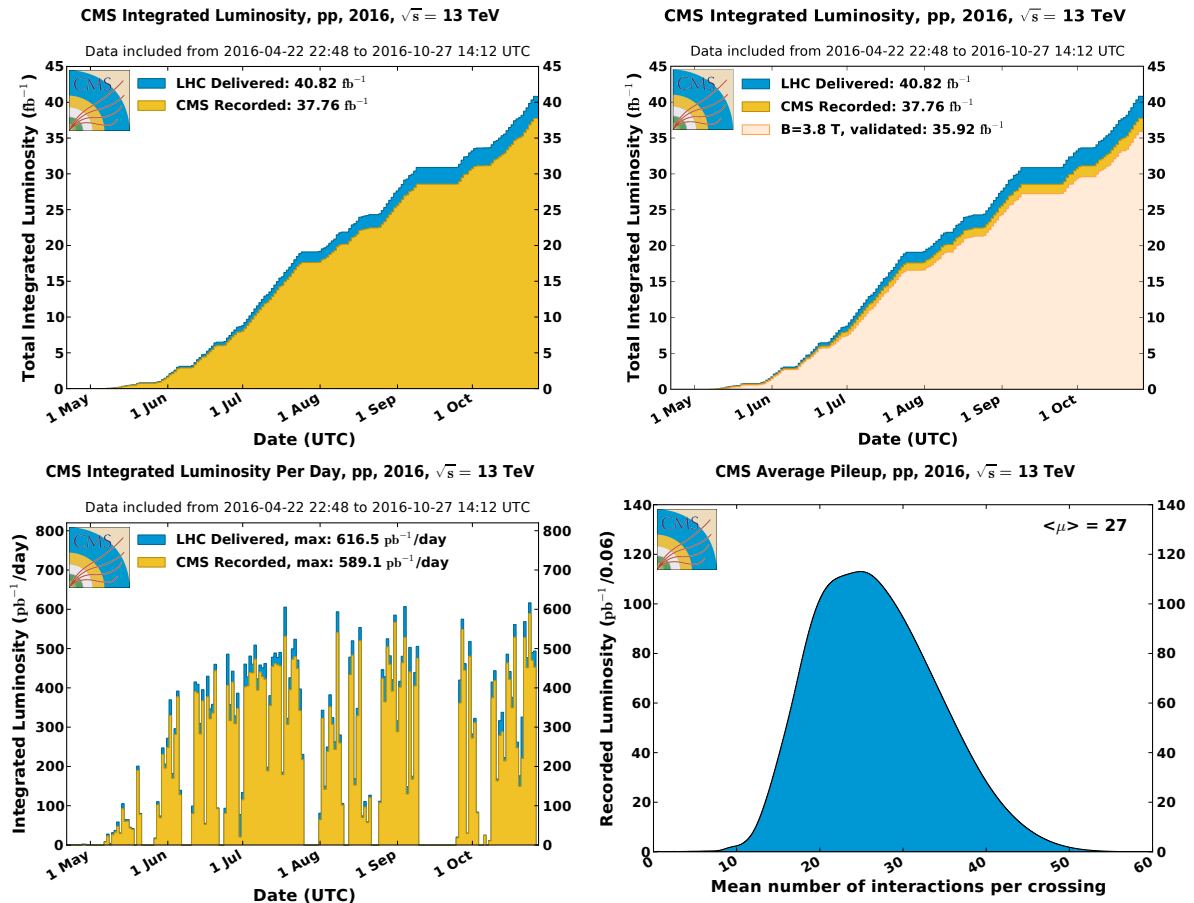


Figure 3.3: Luminosity in 2016 LHC data. Top-left plot: the cumulative integrated luminosity delivered by LHC (in blue) and recorded by CMS (in orange), as a function of the data taken period. Top-right plot: data recorded by CMS and declared as optimal for the physics analyses (in light orange), corresponding to a total integrated luminosity of 35.9  $\text{fb}^{-1}$ . Bottom-left plot: maximum integrated luminosity per day. Bottom-right plot: number of proton interactions per bunch crossing (pile-up).

### 510 3.1.1 Proton-proton interactions

- 511 Proton-proton collisions allow to reach higher energies and luminosities, but the drawback is  
 512 the complexity of the events when compared to electron-positron collisions: not only because  
 513 of the increasing backgrounds due to strong interactions among partons, but also because the  
 514 momenta of the proton partons taking part in the interaction are unknown; not to mention the  
 515 problem of disentangling the tracks of the particles coming from the interesting hard interac-  
 516 tions from the spectator pile-up interactions (in fig. 3.4, 78 proton collisions were happening  
 517 at the same bunch crossing).  
 518 The majority of the LHC events is represented by soft interactions, with low transverse mo-  
 519 mentum transfer, namely elastic and diffractive scatterings. In the so-called hard interactions,  
 520 on the other hand, the transferred momentum among particles is high, allowing to produce  
 521 massive resonant phenomena. These events manifest in peculiar final state signatures that can  
 522 be distinguished from the soft interaction background.

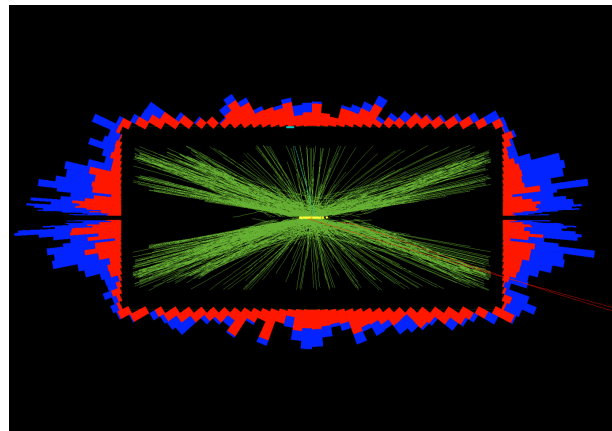


Figure 3.4: 78 events.

523 At high momentum transfer (perturbative regime), a proton can be described as a collection  
 524 of partons, each bringing a fraction  $x$  of the initial beam momentum, whose distribution is  
 525 described by the parton distribution functions (PDF),  $f(x, Q^2)$ , as a function of the Bjorken's  
 526 variable and of the momentum transfer  $Q^2$ . At very high center-of-mass energies (13 TeV), the  
 527 proton masses can be neglected; the available energy in the parton 1 and parton 2 scattering  
 528 is unknown,  $\sqrt{x_1 x_2 s}$ . The total cross-section is given by:

$$\sigma = \int dx_1 f_1(x_1, Q^2) \int dx_2 f_2(x_2, Q^2) \sigma_{12}(x_1 p_1, x_2 p_2, Q^2), \quad (3.4)$$

529 where  $\sigma_{12}$  is the cross-section at parton level, and  $f_1, f_2$  are the parton PDFs. In fig. 3.5, parton  
 530 cross-sections are displayed as a function of the center-of-mass energy.

## 531 3.2 CMS detector

532 The Compact Muon Solenoid (CMS) is a multi-purpose detector built in the LHC ring. It is  
 533 situated in a cavern 100 m underground, near Cessy, in France. It is a cylinder 22 m long, with  
 534 a diameter of 15 m, and a weight of 12500 tons. Its physics programme includes the search  
 535 for the Higgs boson (discovered in 2012), precision measurements of the Standard Model pa-  
 536 rameters and rare decays (physics of beauty quark), and search for new physics beyond the  
 537 standard model (SUSY, exotic phenomena, dark matter, extra dimensions).

538 The CMS detector is structured in many layers of sub-detectors, giving different responses  
 539 depending on the nature and the momentum of the particle passing through. The inner de-  
 540 tectors have been finely segmented in order to afford the high radiation levels and particle  
 541 multiplicity at the interaction point, so that the reduced occupancy of each layer allows to  
 542 measure and distinguish precisely the primary vertices of the hard interactions from the pile-  
 543 up events. A very precise time resolution is vital in order to synchronize all the subsystems  
 544 together.

545  
 546 Fig. 3.6 shows a sketch of the CMS detector. It is longitudinally segmented in the barrel region  
 547 and two endcaps. In the forward region (over the endcaps), where the beam radiation is very  
 548 intense, additional calorimeters have been placed. In fig. 3.7, the mean path of a specific  
 549 particle through the sub-detectors is represented, depending on its flavour.

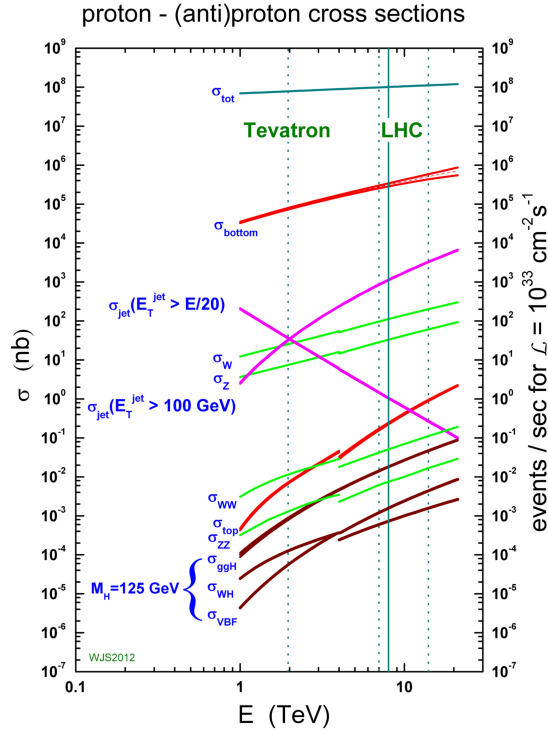


Figure 3.5: Cross-sections and number of expected events in proton-proton collisions, as a function of the center-of-mass energy. Rare phenomena, such as the Higgs boson production, can be observed at the LHC.

### 550 3.2.1 The coordinate system

551 The CMS coordinate system is depicted in fig. 3.8.  $x$  and  $y$  are the coordinates in the transverse  
 552 plane,  $z$  is the longitudinal coordinate. The  $x$  axis points at the center of the LHC ring, the  $y$   
 553 axis points upward, the  $z$  axis is along the beam direction. The azimuthal angle  $\phi$  lays in the  
 554 in the transverse plane, and it is measured starting from the  $x$  axis; the radial coordinate is  $r$ .  
 555 The polar angle  $\theta$  lays in the plane  $rz$ . The transverse component of the 3-momentum,  $\vec{p}_T$ , is  
 556 orthogonal to the beam axis and lays in the plane  $xy$ . The transverse energy is defined as the  
 557 magnitude of  $\vec{p}_T$ :  $E_T = E \sin \theta$ .

558 Two other commonly used variables are the rapidity,  $y$ , and pseudorapidity,  $\eta$ , defined as  
 559 functions of the particle energy  $E$ , the longitudinal component of the momentum  $p_z$  and the  
 560 3-momentum modulus:

$$y = \frac{1}{2} \log \frac{E + p_z}{E - p_z} \quad (3.5)$$

$$\eta = \frac{1}{2} \log \frac{|\vec{p}| + p_z}{|\vec{p}| - p_z} = -\log \tan \frac{\theta}{2}.$$

561 When the considered particle is produced in the forward region, hence at  $\theta = 0$ ,  $\eta \rightarrow \infty$ . When  
 562 the particle is produced in the transverse plane, hence  $\theta = \pi/2$ ,  $\eta = 0$ . At high energies, when  
 563 the masses can be neglected, rapidity and pseudorapidity coincide; these variables are largely  
 564 used at colliders because they are invariant under Lorentz boosts along the beam direction.

# CMS Detector

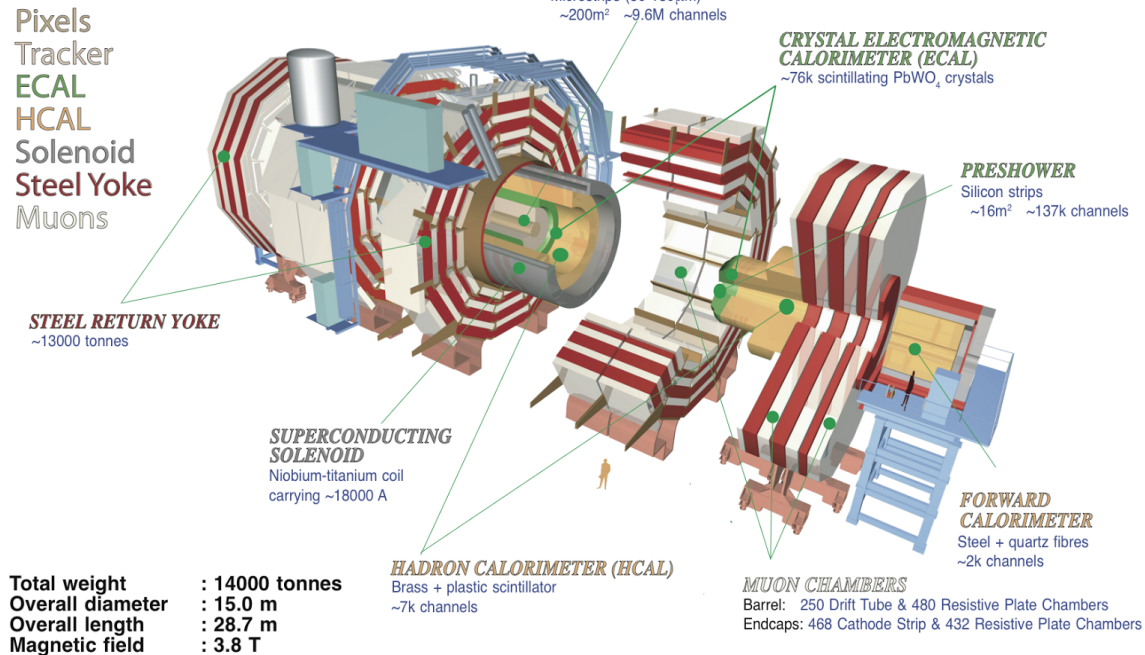


Figure 3.6: The CMS experiment.

### 565 3.2.2 The magnet

566 The CMS superconducting magnet is an hollow cylinder (13 m long, 6 m of diameter, showed  
 567 in fig. 3.9). In the niobium and titanium fibers that constitute the solenoid, an electrical  
 568 current of 19 kA flows, providing a maximum magnetic field of 3.8 T and storing a maximum  
 569 energy of 2.6 GJ. Superconducting conditions are allowed by a liquid helium cooling system,  
 570 keeping the solenoid at 4.5 K. In order to avoid stray fields, the magnetic field lines are closed  
 571 by the return yoke, composed by 10 ktons of magnetized iron blocks, located in the outer  
 572 part of CMS and alternated to the muon chambers. The homogeneous magnetic field inside  
 573 the detector bends the trajectories of the charged particles, allowing the measurement of their  
 574 momenta  $p$ , given the relation with the magnetic field strength  $B$  and the radial coordinate  $R$   
 575 of the trajectory:

$$p[\text{GeV}] = 0.3 \times B[\text{T}] \times R[\text{m}]. \quad (3.6)$$

### 576 3.2.3 The tracking system

577 The CMS tracking system is composed by a cylinder of silicon detectors (2.5 m of diameter  
 578 and 5.8 m length). Their design allows a precise reconstruction of the tracks left by charged  
 579 particles and of the interaction vertices, a fundamental tool to identify heavy quarks (charm,  
 580 beauty) and leptons (taus). Tracker detectors cover a pseudorapidity region of  $|\eta| < 2.5$  and  
 581 have an active area of  $210 \text{ m}^2$ . The two sub-detectors of the tracking system are the pixel

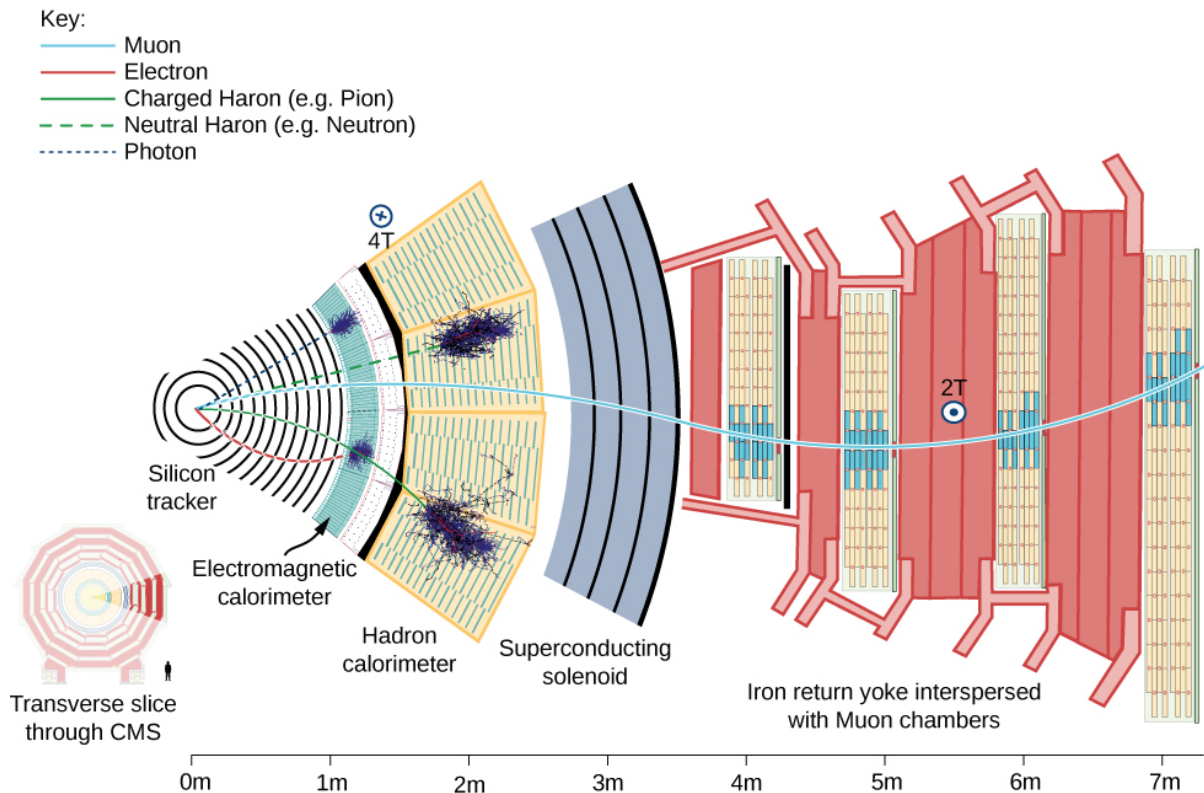


Figure 3.7: Mean path of a particle through the CMS detector. A muon, in light blue, passes through with a bended trajectory, depending on its momentum and charge, triggering signals in all the sub-systems. An electron, in red, leaves a track in the silicon tracker and is absorbed by the electromagnetic calorimeter. A neutral or charged hadron, in green, stops inside the hadronic calorimeter. A photon, dotted blue line, showers in the electromagnetic calorimeter, without leaving any track in the silicon detector.

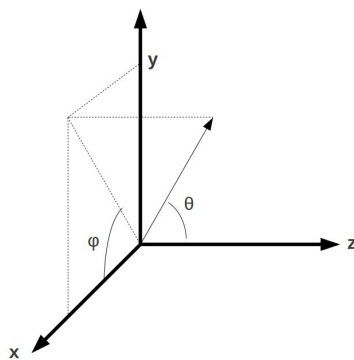


Figure 3.8: CMS coordinate system.

detector, closer to the interaction point, and the strip detector, covering a radius of 0.2 – 1.2 m. The high granularity of the pixels and micro strips allows to keep the occupancy at acceptable levels, given the high multiplicity of the tracks ( $\sim 1 \text{ MHz/mm}^2$ ). The silicon detectors and the electronic cables are cooled down to a temperature of  $\sim 10^\circ \text{ C}$ . The structure of the tracking

## 3.2 CMS detector

---

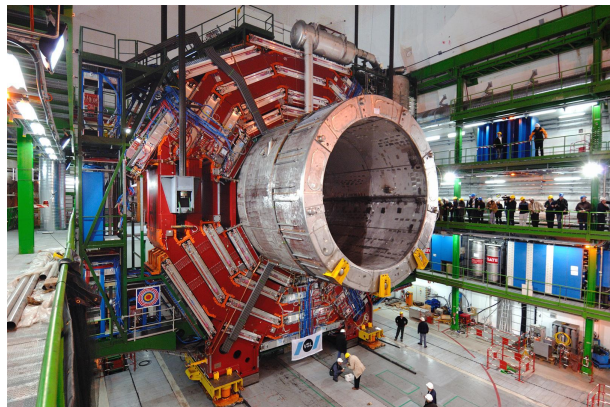


Figure 3.9: Installation of the superconducting solenoid in the CMS cavern.

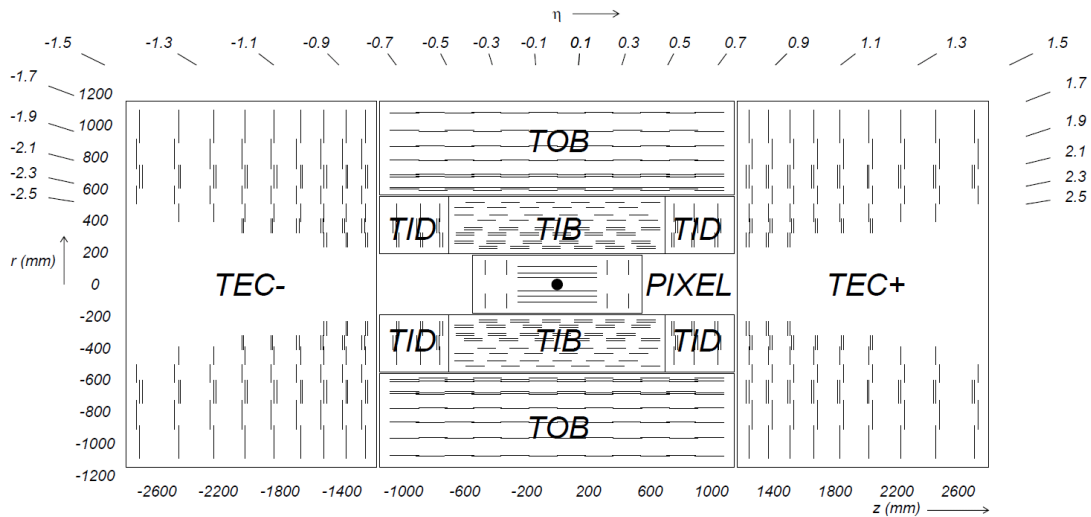


Figure 3.10: The CMS tracking system: the inner pixel detector, close to the interaction point, and the outer strip detector.

586 system is showed in fig. 3.10.

587 **3.2.3.1 The pixel detector**

588 The pixel detector is composed by 66 millions of silicon cells, whose dimensions are  $100 \times$   
 589  $150 \mu\text{m}^2$ ,  $285 \mu\text{m}$  of thickness, placed in 1440 modules. Silicon cells are set in three layers in  
 590 the barrel region and in two disks at each endcap. Barrel modules are disposed parallel to  
 591 the magnetic field, whilst at the endcap they are tilted by about  $20^\circ$ . Pixels allow a spatial  
 592 resolution of  $10 \mu\text{m}$  in the transverse plane, and of  $\sim 20 \mu\text{m}$  along the longitudinal coordinate.  
 593 Their reduced size guarantees an occupancy of  $10^{-4}$  per pixel at each bunch crossing, in high  
 594 luminosity regime.

595 **3.2.3.2 The strip detector**

596 The strip system is divided in the four-layered tracker inner barrel (TIB), covering a region  
 597  $20 < r < 55 \text{ cm}$  with respect to the interaction point, the six-layered tracker outer barrel (TOB),

598 located at  $55 < r < 110$  cm, the three tracker inner disks (TID) and the nine tracker endcaps  
 599 (TEC) at each cylinder base. Given the lower radiation level at higher radii (and hence a lower  
 600 occupancy, around few percent), micro strips are bigger than the pixels. Silicon strips in TIB  
 601 and TID are  $320\ \mu\text{m}$  thick, 10 cm long, and with a pitch ranging from 80 to  $120\ \mu\text{m}$ ; strips in  
 602 TOB and TEC are 25 cm long, with a different thickness ( $320\ \mu\text{m}$  for TID,  $500\ \mu\text{m}$  for TEC)  
 603 and pitch (97–184  $\mu\text{m}$ ). There are 15148 strip modules, and 9.3 million readout channels. The  
 604 strip spatial resolution is about  $20 - 50\ \mu\text{m}$  in the transverse plane and about  $200 - 500\ \mu\text{m}$   
 605 along the longitudinal coordinate.

### 606 3.2.4 The electromagnetic calorimeter

607 The CMS electromagnetic calorimeter (ECAL, shown in fig. 3.11) is a homogeneous detector  
 608 composed by lead tungstate ( $\text{PbWO}_4$ ) scintillating crystals, designed to measure the energy  
 609 deposits of photons and electrons through their electromagnetic showers.  $\text{PbWO}_4$  is transpar-  
 610 ent and dense ( $8.3\ \text{gr}/\text{cm}^3$ ); it has a fast time response (the 85% of the scintillating light is  
 611 emitted at every bunch crossing, namely 24 ns), high scintillating efficiency and radiation re-  
 612 sistance; it has a radiation length is  $X_0 = 0.89\ \text{cm}$  and a Molière radius of  $2.19\ \text{cm}$ . The ECAL is  
 613 divided in the barrel region ( $\eta < 1.479$ , at a radius of 1.3 m) and the endcaps ( $1.479 < \eta < 3$ ).  
 614 The 61200 crystals employed in the barrel region, whose size is  $(22 \times 22)\ \text{mm}^2 \times 23\ \text{cm}$ , have  
 615 a radiation length of  $25.8X_0$ ; the 7324 crystals in the endcaps,  $28.6 \times 28.6\ \text{mm}^2 \times 22\ \text{cm}$ , have  
 616 a radiation length of  $24.7X_0$ . Before the endcaps, on each side, a pre-shower detector is in-  
 617 stalled: it is composed by two disks of lead absorber and two layers of silicon strips, up to a  
 618 radiation length of  $3X_0$ . It has been designed to distinguish the photons coming from the  $\pi^0$   
 619 decay from the rare Higgs decay  $H \rightarrow \gamma\gamma$ . The readout and amplification of the scintillating  
 620 light, performed by avalanche photodiodes in the barrel and by vacuum phototriodes in the  
 621 endcaps, requires a stable temperature of  $18^\circ\ \text{C}$ , mantained by a water cooling system.

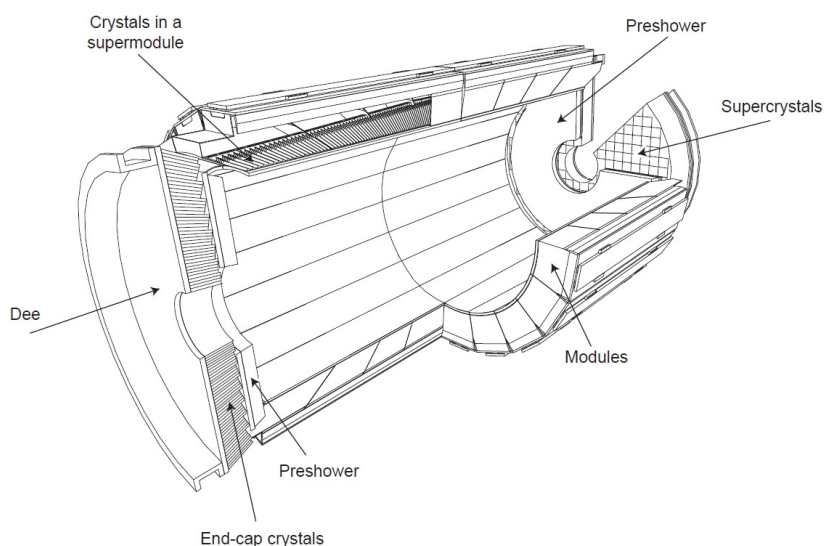


Figure 3.11: The CMS electromagnetic calorimeter.

### 3.2 CMS detector

---

622 The energy resolution of the calorimeter is parametrized as:

$$\left(\frac{\sigma}{E}\right)^2 = \left(\frac{S}{\sqrt{E}}\right)^2 + \left(\frac{N}{E}\right)^2 + C^2, \quad (3.7)$$

623 where  $S = 0.028 \text{ GeV}^{\frac{1}{2}}$  is the stochastic term,  $N = 0.12 \text{ GeV}$  is related to noise contribution,  
624 and  $C = 0.003$  is a constant term depending on the calibration.

#### 625 3.2.5 The hadronic calorimeter

626 The hadronic calorimeter (HCAL, displayed in fig. 3.12) is a sampling calorimeter, composed  
627 by brass and plastic scintillator layers. It has been designed in order to guarantee a good  
628 hermeticity, allowing to perform a precise measurement of the missing transverse energy. It is  
629 located within the electromagnetic calorimeter and the solenoid, covering a region of  $|\eta| < 1.3$   
630 in the barrel, and  $1.3 < |\eta| < 3$  in the endcaps. Brass is non-magnetic and has short interac-  
631 tion length (16.4 cm): the 60 mm thick absorber layers used in the barrel allow to reach 5.6  
632 interaction lengths at  $\eta = 0$  and 10.8 interaction lenghts at  $\eta = 1.3$ ; the 80 mm thick layers in  
633 the endcaps reach 11 interaction lenghts. An additional calorimetric layer has been installed  
634 out of the solenoid, in order to reach 11.8 interaction lenghts in the barrel region. The scin-  
635 tillation light, typically in the blue-violet region of the electromagnetic spectrum, is collected  
636 by wavelenght-shifter fibers, translated and amplified by multi-channel hybrid photodiodes,  
637 proportionally to the magnitude of the energy deposits. An additional hadronic calorimeter  
638 has been placed in the forward region,  $3 < |\eta| < 5.2$ , at 11.2 m from the interaction point.  
639 It has beeen designed to afford the high levels of radiations: it is composed by 55 mm thick  
640 absorber layers of stainless-steel, and quartz fibers, able to detect the Cherenkov scintillating  
641 light of the charged particles of the hadronic showering. A longitudinally segmentation allow  
642 to distinguish hadronic particles from electromagnetic components. The energy resolution of  
643 the hadronic calorimeter is:

$$\left(\frac{\sigma}{E}\right) \approx \frac{a}{\sqrt{E}} \oplus b\%, \quad (3.8)$$

644 where  $a = 65\%$  in the barrel region,  $85\%$  in the endcaps,  $100\%$  in the forward region, and  
645  $b = 5\%$ .

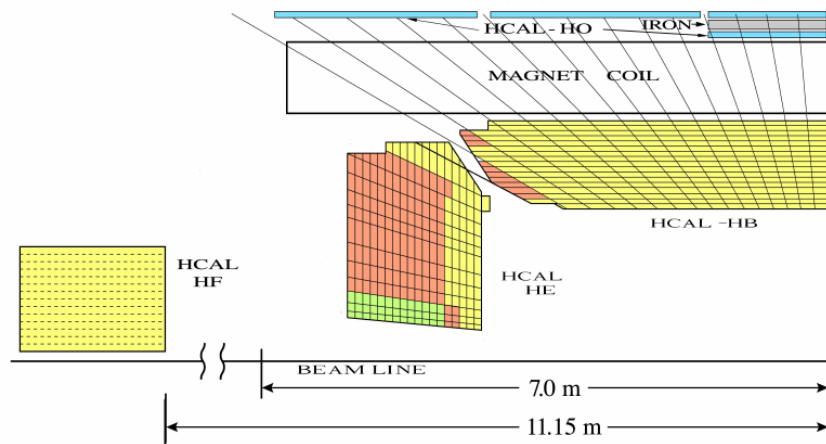


Figure 3.12: The CMS hadronic calorimeter.

### 3.2.6 The muon system

The outer system of the CMS experiment consists into gas detectors for identifying muons, that are located between the iron return yokes, designed to close the magnetic field generated by the solenoid. In the barrel region, where a smaller number of muons is expected and the magnetic field is less strong, Drift Tubes (DT) detectors are installed. In the endcaps, where the flux of particles is larger, Cathod Strip Chambers (CSC) are used, and disposed in three disks. CSCs are designed to allow faster responses, higher granulatiy and radiation resistance. Resistive Plate Chambers (RPC) are installed both in the barrel and in the endcaps as additional triggering system. The geometry of the muon system is showed in fig. 3.13; it consists of 250 DTs, 530 CSCs, 610 RPCs, and it covers a region  $|\eta| < 2.4$ .

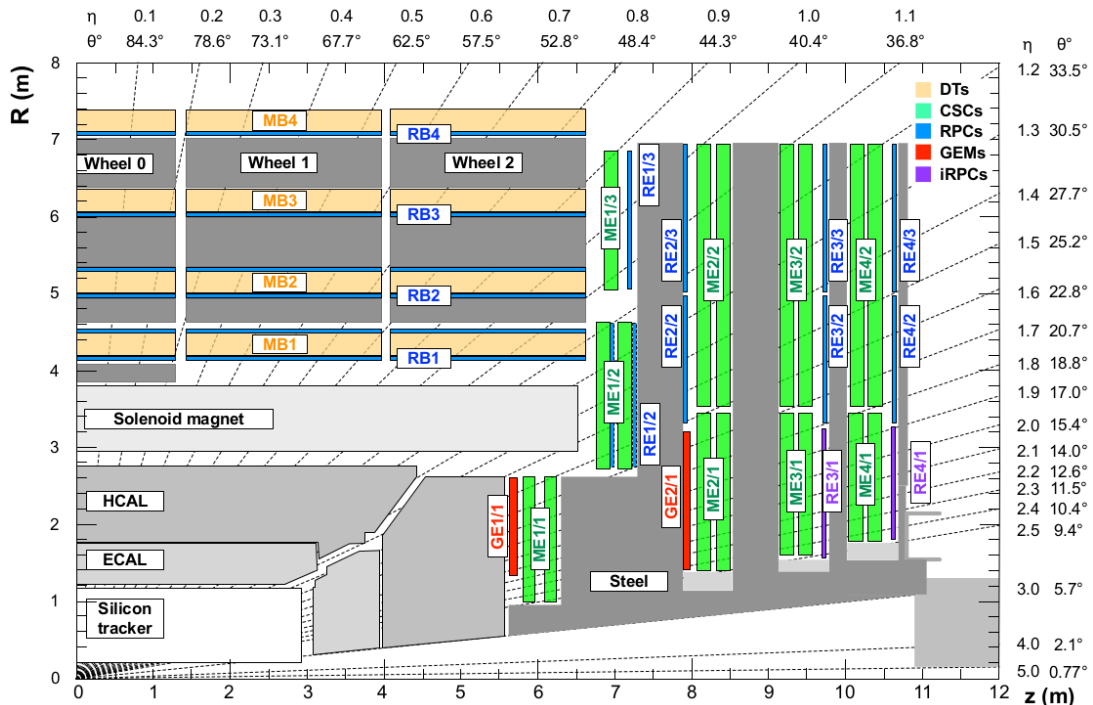


Figure 3.13: Section of CMS detector, in the plane  $r z$ , parallel to the beamline, that emphasizes the location of the muon detectors, in particular: Drift Tubes (DT, in yellow); Cathode Strip Chambers (CSC, in green); Resistive Plate Chambers (RPC, in blue).

#### 3.2.6.1 The Drift Tubes

Drift Tube detectors cover a region of  $|\eta| < 1.2$  and are arranged in four stations, segmented along the beam line in five wheels. The basic element of the detector is the cell, that has a size  $42 \times 13 \text{ mm}^2$ . Each cell is filled with a gas mixture (85% argon, 15%  $\text{CO}_2$ ), in which the process of ionization takes places; the ionization electrons drift from the  $50 \mu\text{m}$  thick steel anodic wire, in the center of the cell, towards the aluminium cathodic strips, located at its edge. Additional electrodes on the surface of the cells allows to shape the electric field, in order to make the drift speed of the electrons uniform: the muon position is then extrapolated from the measurement of the drift time. Every station is composed by three cells superlayers. In the inner and the outer superlayers, the cells are oriented such in a way that the anodic

## 3.2 CMS detector

---

666 wire is located along the  $z$  axis, in order to measure the  $\phi$  coordinate. In the intermediate  
667 superlayer, wires are parallel to the radial coordinate, hence they can measure the  $z$  position.  
668 The spatial resolution of the system is  $100 \mu\text{m}$  in the  $r\phi$  plane, 1 mrad in the  $\phi$  coordinate, and  
669  $150 \mu\text{m}$  in the longitudinal  $z$  coordinate.

670 **3.2.6.2 The Cathode Strip Chambers**

671 Cathode Strip Chambers cover a region of  $0.9 < |\eta| < 2.4$ , overlapping with the DT in the  
672 pseudorapidity range  $0.9 < |\eta| < 1.2$ . The anodic wires inside each CSC are located into six  
673 planes, with the aim of measuring the radial coordinate; the wire planes are perpendicularly  
674 crossed by cathodic strips, disposed along the radial direction to measure the  $\phi$  coordinate.  
675 Ionization electrons produced by muons passing through the gas mixture in the chambers  
676 migrate towards the anode, inducing a charge distribution on the cathodes, from which the  
677 azimuthal coordinate can be reconstructed. The spatial resolution in the  $r$  coordinate is  $200$   
678  $\mu\text{m}$ , and it is  $75 - 150 \mu\text{m}$  in the  $r\phi$  plane. CSCs are arranged in four disks and in three  
679 concentric rings.

680 **3.2.6.3 The Resistive Plate Chambers**

681 Resistive Plate Chambers (RPC) are located both in the barrel (disposed in six layers) and in  
682 the endcap region (three layers), up to a pseudorapidity of  $|\eta| < 1.6$ . These gas detectors  
683 are charged at very high voltages, in order to work in the avalanche ionization mode. The  
684 plastic resistive plates are equipped with readout strips. The spatial resolution of the detector  
685 is low (1-2 cm), but the fast timing response (2-3 ns) and good time resolution (1 ns) allow to  
686 employ RPCs as an additional triggering system and to profit of a precise measurement of the  
687 bunch-crossing time.

688 **3.2.7 The trigger system and data acquisition**

689 The CMS trigger system has been designed considering the high instantaneous luminosity,  
690 such that it can provide a fast response and it allows to reduce the nominal event rate of  
691 40 MHz in proton proton collision. The complexity of the CMS detector and the very high  
692 number of readout channels result into a huge amount of data per event, approaching the  
693 order of few MB per bunch crossing, hence 40 TB per second. The handling and the recording  
694 of data is currently limited at the order of  $\sim 100$  Hz; hence, applying online selections to  
695 skim the events that are going to be written on tape, without rejecting interesting signals of  
696 hard processes and rare phenomena becomes a crucial and challenging point for every data  
697 analysis. Events are filtered by trigger selections at different levels: the Level-1 (L1) trigger  
698 is an hardware device, that allows to reduce the event rate from 40 MHz to the order of 100  
699 kHz; the High Level Trigger (HLT) is a set of software algorithms that skims the event rate  
700 down to few hundred Hz. Once the trigger decisions are taken, the final events are handled  
701 by the Data Acquisition System (DAQ), that collects the informations coming from to the  
702 subdetectors and sends them to the storage devices.

703 **3.2.7.1 The Level-1 trigger**

704 The L1 trigger is an hardware device composed by customized electronics, and it accesses  
705 the informations coming from the calorimeters and the muon system, while the tracker is not

706 considered given the excessively large bandwidth needed by its readout channels. The L1  
 707 trigger perform a first raw local reconstruction of each object, called “trigger primitive”. The  
 708 L1 trigger is composed by three subsystems: the calorimeter trigger, the muon trigger (divided  
 709 in three independent sub-subsystems for each muon subdetector, namely DTs, RPCs and  
 710 CSCs), and the global trigger, that combines the informations of the former subsystems. The  
 711 best quality trigger primitives reconstructed by the calorimeter and muon detectors (namely,  
 712 roughly reconstructed electrons, photons, muons, jets, jets coming from the hadronic decays  
 713 of tau leptons, and missing energy) are handled by the global trigger, who takes the decision  
 714 of discarding or keeping the event every 3.2  $\mu$ s. The simplest trigger selections require the  
 715 presence of a single object, whose energy or transverse momentum is higher than a certain  
 716 threshold; more complicated triggers involve multiple objects or geometrical selections, that  
 717 can be performed in parallel up to 128 simultaneous requirements.

718 **3.2.7.2 The High Level Trigger**

719 The HLT skims the L1 output rate down to few hundreds of Hz by applying a set of algo-  
 720 rithms implemented in the same software used for the offline analysis, consisting in the event  
 721 reconstructions exploiting the whole informations coming from all subdetectors. The comput-  
 722 ing time is still a crucial factor, hence selections applied to HLT physics objects are generally  
 723 less accurate than those of the offline analysis; furthermore, HLT can discard the event even  
 724 before its full reconstruction (*i.e.* by looking only at certain region of the detectors). Events  
 725 filtered by the HLT decisions are assigned to precise trigger paths and recorded in precise  
 726 categories of datasets.

727 **3.2.7.3 Data acquisition, computing and storage**

728 The DAQ system deals with the storage, transfer and handling of the data collected by CMS;  
 729 it also supports and stores the data simulations and calibrations of the subdetectors. The  
 730 CMS computational resources are located in worldwide distributed data nodes, called Tiers.  
 731 The CMS software (CMSSW) is based on an object oriented architecture (mainly C++). The  
 732 basic unity of every data, both real and simulated ones, is the Event, that could contain very  
 733 rough informations (RAW data format) or higher level refined objects (AOD, Analysis Object  
 734 Data) where all the calibrations and corrections needed to properly deal with the final physics  
 735 objects are already in place. Data are handled by C++ or python modules, and the outputs  
 736 are written in ROOT files. [cittazione]

737 **3.2.8 Particle Flow event reconstruction**

738 – ref from paper The global event reconstruction at CMS relies on the particle flow (PF) [69,  
 739 70] algorithm, which reconstructs and identifies each individual particle with an optimized  
 740 combination of informa- tion from the various elements of the CMS detector. The energy of  
 741 photons is directly obtained from the ECAL measurement, while the energy of electrons is  
 742 determined from a combina- tion of the electron momentum at the primary interaction vertex  
 743 as determined by the tracker, the energy of the corresponding ECAL cluster, and the energy  
 744 sum of all bremsstrahlung pho- tons spatially compatible with originating from the electron  
 745 track. The momentum of muons is obtained from the curvature of the corresponding track.  
 746 The energy of charged hadrons is determined from a combination of their momentum mea-

### 3.2 CMS detector

---

747 sured in the tracker and the matching ECAL and HCAL energy deposits, and the energy  
748 of neutral hadrons is obtained from the corresponding ECAL and HCAL energy. The core  
749 of the particle flow reconstruction technique is the algorithm used to link the signals of the  
750 individual subdetectors. The association criteria is purely geometrical. The aim is a full recon-  
751 struction of each single particle, while reducing any possible double counting from different  
752 detectors. Given the granularity of the calorimeters, energy deposits and tracks are linked  
753 if their trajectory intersects one of the calorimetric cells, and likewise clusters in the ECAL  
754 pre-shower, ECAL and HCAL are linked if the cluster position is compatible in the  $\phi$ , plane  
755 between the extrapolated track position and the cluster position.

756 The particle-flow event reconstruction aims at reconstructing and identifying all sta- ble  
757 particles in the event, i.e. electrons, muons, photons, charged hadrons and neu- tral hadrons,  
758 by mean of an optimized combination of informations from all CMS sub- detectors. The  
759 algorithm is described in detail in References [4446] where information on its commissioning  
760 with early data are also provided. The CMS PF algorithm relies on a efficient and pure track  
761 reconstruction, on a clustering algorithm able to disentangle overlapping showers, and on an  
762 efficient link procedure to connect together the deposits of each particle in the sub-detectors.  
763 Tracks are extrapolated through the calorimeters: if they fall within the boundaries of one  
764 or several clusters, the clusters are associated to the track. The set of track and cluster(s)  
765 constitute a charged hadron and are not con- sidered anymore in the rest of the algorithm.  
766 The muons are identified beforehand so that their track does not give rise to a charged hadron.  
767 The electrons are more difficult to deal with. Indeed, due to the frequent Bremsstrahlung  
768 photon emission, a specific track reconstruction (the GSF already discussed in Section 2.2.3.1)  
769 is needed as well as a ded- icated treatment to properly attach the photon clusters to the  
770 electron and avoid energy double counting. Once all the tracks are treated, the remaining  
771 clusters result in photons in case of the electromagnetic calorimeter (ECAL), and in neutral  
772 hadrons in the case a hadron calorimeter (HCAL) cluster is matched to an ECAL cluster. Once  
773 all the deposits of a particle are associated, its nature can be assessed, and the information of  
774 the sub- detectors combined to determine optimally its four-momentum. In case the calibrated  
775 calorimeter energy of the clusters, which is simply a linear combination of the ECAL and  
776 HCAL energy deposits, associated to a track is found to be in excess with respect to the  
777 track momentum at more than one sigma, the excess is attributed to an overlapping neu-  
778 tral particle (photon or hadron), carrying an energy corresponding to the difference of the  
779 two measurements. The resulting list of particles, namely charged hadrons, photons, neutral  
780 hadrons, electrons and muons, is then used to reconstruct the jets, the missing transverse  
781 energy, to reconstruct and identify the from their decays products and to measure the isolation  
782 of the particles. The association used in the linking stage is purely geometrical: tracks are  
783 linked to calori- metric clusters if their trajectory intersects one of the calorimetric cells of the  
784 cluster; and likewise clusters in the ECAL preshower, ECAL and HCAL are linked if the cluster  
785 posi- tion measured in the finer granularity subdetector lies within the envelop of the cluster  
786 in the coarser granularity subdetector. In order to account for uncertainties from mul- tiple  
787 scattering in the track extrapolation and on the estimated position of the shower maximum in  
788 the calorimeters, a geometrical tolerance of the size of one calorimeter cell is included when  
789 defining links; this tolerance can also account for gaps and cracks in the calorimeters. By  
790 design, the linking algorithm is simple and robust, as it does not rely on the precise knowledge  
791 of the position resolution in each subdetector. Special- ized algorithms are used for linking  
792 tracks to recover bremsstrahlung clusters in the case of electrons by considering tangents to

793 electron trajectories at the crossing points with the tracker layers. Blocks of one or more linked  
794 objects are then processed to identify and reconstruct particle candidates. Isolated electrons  
795 and muons are selected first, and reconstructed using the dedicated algorithms developed  
796 for them; similarly, non-isolated tracks which satisfy tight muon identification criteria are  
797 immediately identified as muons. Charged hadrons are identified as tracks in the inner  
798 tracker, normally linked to calorimetric deposits if the particle  $p_T$  is sufficient for the trajectory  
799 to reach the calorimeters. If the momentum measurements from the track and calorimeter are  
800 compatible, after accounting for non-linearities and zero suppression effects, the best energy  
801 determination is obtained as a combination of the two. If the track momentum significantly  
802 exceeds the measured calorimetric energy, the particle is identified as muon if it satisfies very  
803 loose muon identification criteria; otherwise, tight track quality requirements are applied  
804 to reject mis-reconstructed tracks. If instead an excess of calorimetric energy deposition is  
805 found with respect to the momentum of the associated track, e.g. in the case of collimated  
806 hadronic jets, the residual energy is identified as a photon or a neutral hadron. Additional  
807 photons and neutral hadrons are also identified from calorimetric deposits not linked to any  
808 track.

809 **3.2.9 Physics objects**

810 **3.2.9.1 Track and vertex reconstruction**

811 **3.2.9.2 Electron reconstruction**

812 **3.2.9.3 Photon reconstruction**

813 **3.2.9.4 Muon reconstruction**

814 L'intero sistema misura in maniera "standalone" l'impulso con una risoluzione in  $p_T$  di circa  
815  $\Delta p_T/p_T \approx 8 - 15\%$  per muoni di  $p_T = 10 \text{ GeV}/c$  e di  $\Delta p_T/p_T \approx 20 - 40\%$  per muoni di  $p_T = 1$   
816 TeV/c. Combinando con la misura nei rivelatori al silicio la risoluzione passa rispettivamente  
817 all'1% e al 7 – 16%.

818

819 **3.2.9.5 Jet reconstruction**

820 **3.2.9.6 Tau reconstruction**

821 **3.2.9.7 Missing transverse energy reconstruction**

822 **3.2.9.8 b-quark tagging**

823 **3.3 ATLAS, ALICE, LHCb detectors**

824 **3.3.1 ATLAS**

825 ATLAS (A Toroidal LHC ApparatuS) is a multi-purpose experiment, that shares the same  
826 scientifical aims of CMS. The simultaneous observation of an Higgs boson-like particle at  
827 the two experimental facilities represented an irrefutable proof of the discovery of the Higgs  
828 boson.

829 ATLAS has a cylindrical shape (diameter of 25 m, length of 46 m) and weights 7000 tons. Like  
830 CMS, ATLAS is composed by many sub-detectors: trackers, calorimeters and muon system.

### 3.3 ATLAS, ALICE, LHCb detectors

---

831 The ATLAS magnetic field is provided by a solenoid, located inside the cylinder, and a big  
832 toroid, located outside the sub-detectors, able to reach a magnetic field of 2 T at the interaction  
833 point. The main differences among the two experiments are listed below.

- 834 • *Tracker* – the CMS tracker has a better  $p_T$  resolution (mainly due to the higher magnetic  
835 field):  $\sigma_{p_T}/p_T \approx 5 \cdot 10^{-4} p_T + 0.01$  at ATLAS;  $\sigma_{p_T}/p_T \approx 1.5 \cdot 10^{-4} p_T + 0.005$  at CMS.
- 836 • *Electromagnetic calorimeter* – the CMS electromagnetic calorimeter is completely enclosed  
837 inside the solenoid, whilst ATLAS calorimeter is outside of the solenoid. The particles  
838 going through the solenoid suffer an energy loss and a consequent deterioration of  
839 the energy resolution. The CMS ECAL has an energy resolution of  $\sigma_E/E \approx 3\%/\sqrt{E}$ ;  
840 the ATLAS calorimeter has a sandwich structure (liquid argon and lead layers) and a  
841 resolution of  $\sigma_E/E \approx 10\%/\sqrt{E}$ .
- 842 • *Hadronic calorimeter* – the CMS HCAL is partly inside the solenoid, partly outside, de-  
843 pauperating the resolution. The ATLAS hadronic calorimeter (made of iron and plastic  
844 scintillator tiles) has an energy resolution  $\sigma_E/E \approx 50\%/\sqrt{E} + 0.03$  GeV; CMS HCAL has  
845 a resolution of  $\sigma_E/E \approx 100\%/\sqrt{E} + 0.05$  GeV.
- 846 • *Muon system* – the peculiar geometry of the ATLAS muon system allows a better reso-  
847 lution of the standalone measurement of the muon momenta (*i.e.*, without using tracker  
848 and calorimeters), that is around 10% at 1 TeV. CMS has better performance when com-  
849 bining the informations coming from the inner detectors (7% at 1 TeV against the 35%  
850 for the standalone measurement).

851 **3.3.2 ALICE**

852 ALICE (A Large Ion Collider Experiment) studies the heavy ion collisions (lead-lead) or  
853 proton-ion in order to explore the physics of the hadrons in high density (or temperature)  
854 regimes, when a new state of matter appears, the so-called quark-gluon plasma (QGP). The  
855 QGP played a crucial role in the very first instants of life of the universe.

856 **3.3.3 LHCb**

857 LHCb (Large Hadron Collider beauty) is a detector designed to study the b quark properties,  
858 in particular the CP violation and other rare phenomena involved in b hadrons. The final aim  
859 of these measurements is trying to solve the matter-antimatter asymmetry problem.

860 The three detectors are depicted in fig. 3.14–3.16.

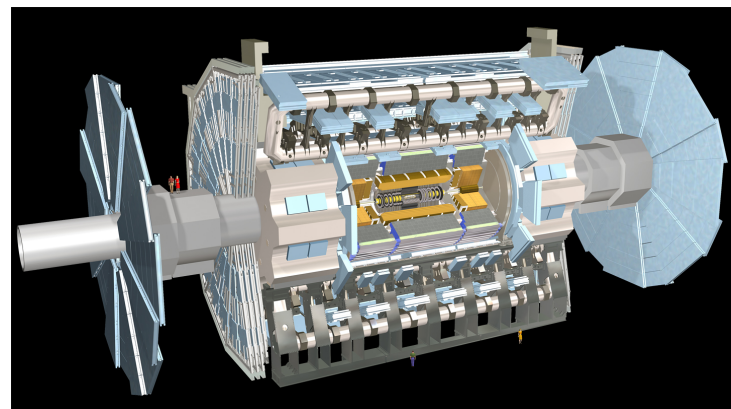


Figure 3.14: The ATLAS experiment.

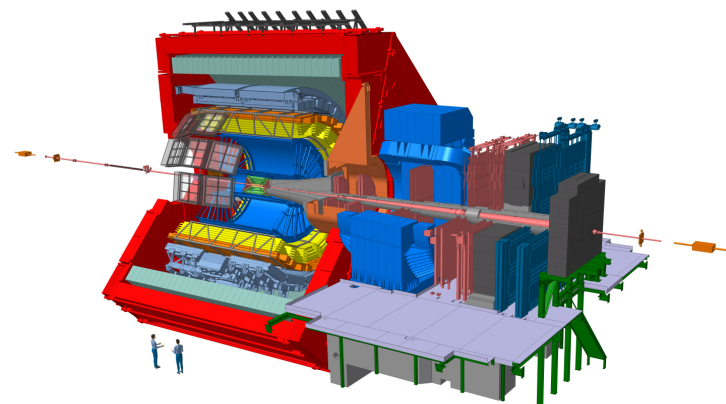


Figure 3.15: The ALICE experiment.

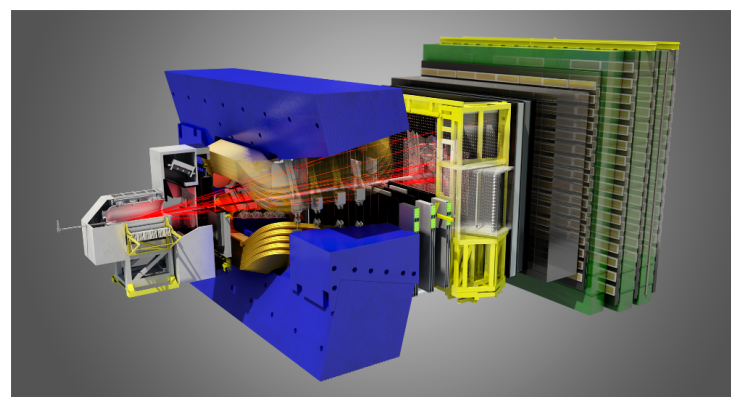


Figure 3.16: The LHCb experiment.

# Search for diboson resonances in the $ZV \rightarrow \nu\bar{\nu}q\bar{q}$ final state

864 Brief intro to the analysis

<sup>865</sup> **4.1 Data and Monte Carlo samples**

## 4.2 Event selection

---

### 4.2 Event selection

In this section, a list of the physics objects used in the analysis is presented, together with performance and validation plots.

The objects are selected according to the standard Run2 recommendations provided by the various POGs for the Summer16 (25ns) MiniAOD-v2 (Moriond recommendations).

The version of CMSSW used for the analysis is CMSSW\_8\_0\_25.

#### 4.2.1 Vertex and Pile-up

##### How the vertices and pile-up are reconstructed

Due to pileup several primary vertices are typically reconstructed in an event. The primary vertex of the event is defined as the one with the highest sum of transverse momenta  $\sum p_T^2$  of clustered physics objects associated to it, which passes the following selections:

- number of degrees of freedom  $N_{DoF} > 4$
- vertex position along the beampipe  $|z_{vtx}| < 24\text{cm}$
- vertex distance with respect the beam pipe  $d_0 < 2\text{cm}$

where  $z_{vtx}$  and  $d_0$  are the distance along and perpendicular to the beam line of the vertex with respect the nominal interaction point  $(0, 0, 0)$ .

The data sample contains a significant number of additional interactions per bunch crossing, an effect known as pileup (PU).

The Summer16 v2 MINIAOD Monte Carlo samples are generated simulating the PU conditions, using the 25ns asymptotic PU scenario. Nevertheless, the MC PU description does not match exactly the conditions in data, and there is therefore the need to reweight the simulated events in order to improve the agreement with the data.

The MC samples are reweighted using the standard CMS PU reweighting technique [39,40] assuming a total inelastic cross section of  $\sigma_{in} = 69\,200\mu\text{b}$ .

The comparison between the distributions of primary vertices in data and MC after the PU reweighting is applied is shown in Figure 4.1 for an event selection (called inclusive selection) requiring large amount of  $E_T^{\text{miss}}$  recoiling against an AK8 fat jet (Tab. ??).

Figure 4.1: Primary vertices distributions after reweighting with the official recipe and  $\sigma_{in} = 69\,200\mu\text{b}$ .

#### 4.2.2 Electrons

##### How the electrons are reconstructed

Electrons are reconstructed from energy deposits in the ECAL matched to tracks reconstructed in the silicon tracker. The electron trajectories are reconstructed using a dedicated modeling of the electron energy loss and fitted with a Gaussian sum filter. Electrons used in this analysis are required to pass the Particle Flow criteria, and to fall in the ECAL pseudorapidity fiducial range ( $|\eta| < 2.5$ ).

The electron identification used in this analysis is based on the “cut-based” Id defined by the EGamma POG for the Summer16 25ns [41], and suggested also for the usage in 80X

for the so-called Moriond dataset. Isolation cuts are already applied within the cut-based Id definitions, therefore no additional Isolation cut is required. In the isolation definition the effect of PU is considered by taking into account the energy deposits in the calorimeter, estimated through the so-called  $\rho$ -area method, by subtracting the median energy density in the event  $\rho$  multiplied by electron effective area. The isolation value is computed in a  $\Delta R$  cone of 0.3 centered along the lepton direction.

Since in this analysis we are aiming at a final state without any lepton, every electron identified with *veto* cut-based Id, transverse momentum  $p_T > 10$  GeV is vetoed. The detailed set of cuts to define a *veto* cut-based Id electron are reported in the Table 4.1.

	Electrons		Veto	
		EB	EE	
$\sigma_{ij\eta\eta}$	<	0.0115	0.037	
$\Delta\eta_{in}^{seed}$	<	0.00749	0.00895	
$\Delta\varphi_{in}$	<	0.228	0.213	
$H/E$	<	0.356	0.211	
relIso (EA)	<	0.175	0.159	
$ 1/E - 1/p $	<	0.299	0.15	
$ d_0 $	<	0.05	0.10	
$ d_z $	<	0.10	0.20	
missing hits	$\leq$	2	3	
conversion veto	yes		yes	

Table 4.1: Summer16 cut-based selection for 25ns conditions. EB: barrel cuts ( $|\eta_{\text{supercluster}}| \leq 1.479$ ); EE: endcap cuts ( $|\eta_{\text{supercluster}}| > 1.479$ )

Scale factors for electron identification (including isolation) are provided by Egamma POG, derived for 80X (Moriond 17 recommendation), that can be found in [42].

### 4.2.3 Muons

#### How the muons are reconstructed

In the standard CMS reconstruction for  $pp$  collisions, muon tracks are first reconstructed independently in the inner tracker (tracker track) and in the muon system (standalone-muon track). Based on these objects, two reconstruction approaches are used [43]: *Global Muon* (outside-in) and *Tracker Muon* (inside-out).

*reconstruction (outside-in)*: for each standalone-muon track, a matching tracker track is found by comparing parameters of the two tracks propagated onto a common surface, and a global-muon track is fitted combining hits from the tracker track and standalone-muon track, using the Kalman-filter technique [44]. At large transverse momenta,  $p_T > 200$  GeV, the global-muon fit can improve the momentum resolution compared to the tracker-only fit.

*reconstruction (inside-out)*: in this approach, all tracker tracks with  $p_T > 0.5$  GeV and the total momentum  $p > 2.5$  GeV are considered as possible muon candidates and are extrapolated to the muon system taking into account the magnetic field, the average expected energy losses, and multiple scattering in the detector material. If at least one muon segment (i.e., a short

## 4.2 Event selection

---

928        track stub made of DT or CSC hits) matches the extrapolated track, the corresponding  
929        tracker track qualifies as a Tracker Muon.

930        Tracker Muon reconstruction is more efficient than the Global Muon reconstruction at low  
931        momenta,  $p_T \lesssim 5\text{GeV}$ , because it requires only a single muon segment in the muon system,  
932        whereas Global Muon reconstruction is designed to have high efficiency for muons penetrat-  
933        ing through more than one muon station and typically requires segments in at least two muon  
934        stations. Thanks to the high tracker-track efficiency and a very high efficiency of reconstruct-  
935        ing segments in the muon system, about 99% of muons produced in  $pp$  collisions and having  
936        sufficiently high momentum are reconstructed either as a Global Muon or a Tracker Muon,  
937        and very often as both. Muons reconstructed only as standalone-muon tracks have worse  
938        momentum resolution and less favorable collision muon to cosmic-ray muon ratio than the  
939        Global and Tracker Muons and are usually not used in physics analyses.

940        Muons are usually based on the *Particle Flow Muon* selection, considering Global Muon or  
941        a Tracker Muon candidates and by applying minimal requirements on the track components  
942        in the muon system and taking into account a matching with small energy deposits in the  
943        calorimeters.

For muons reconstructed using the PF algorithm, the standard muon isolation is defined as the ratio of the  $p_T$  sum of all charged and neutral particle-flow candidates in the event within a cone with a radius of  $\Delta R = 0.4$  centered along the lepton direction. Corrections in order to reduce the PU contamination are also applied, using the  $\Delta\beta$  method. Charged candidates falling into the cone that are not compatible with the primary vertex are removed from the sum. Additionally, the neutral contribution from PU is estimated to be half the one coming from charged candidates, and this quantity is also subtracted from the total. Eventually, the scalar sum is divided by the lepton  $p_T$  itself. The general formula for the standard *particle-flow* isolation is then:

$$I_{rel} = \left[ \sum p_T^{\text{ch had}} + \max(\sum p_T^{\text{neu had}} + \sum p_T^\gamma - 0.5 \cdot \sum p_T^{\text{pu ch had}}, 0) \right] / p_T^\ell$$

944        where  $\sum p_T^{\text{ch had}}$  is the sum of the transverse momenta of the charged hadrons,  $\sum p_T^{\text{neu had}}$  is  
945        the sum of transverse energies of the neutral hadrons,  $p_T^\gamma$  is the sum of the transverse energy  
946        of particle flow photons and  $\sum p_T^{\text{pu ch had}}$  is the sum of transverse momenta of the charged  
947        particles in the cone of interest but with particles not originating from the primary vertex (for  
948        pileup corrections).

949        In the VZ event selection, all muons identified with the Loose standard id,  $p_T$  over 10 GeV,  
950        PF isolation below 0.25,  $|\eta| < 2.4$  are vetoed.

951        Scale factors for muon identification and isolation are centrally provided as a function of  
952        the muon  $p_T$  and  $\eta$  by the Muon POG [45], and are applied consistently in the analysis.

### 953 4.2.4 Taus

#### 954 How the taus are reconstructed

955        The presence of hadronically-decaying taus only act as veto for the events both in the sig-  
956        nals and in the control regions to suppress electroweak backgrounds. The selection criteria  
957        for taus are  $p_T > 18\text{ GeV}$  and  $|\eta| < 2.3$ . The Run2 TauPOG recommended identification cri-  
958        teria [46] (`decayModeFinding`, `byLooseCombinedIsolationDeltaBetaCorr3Hits`) are required  
959        and applied in order to identify possible tau candidates.

---

 960 **4.2.5 Photons**

 961 **How the photons are reconstructed**

962 As in the case of tau leptons, a photon veto is applied in the analysis both for the signal  
 963 and the control regions. Events are rejected if they contains one (or more) photon with  $p_T > 15$   
 964 GeV,  $|\eta| < 2.5$ , passing the Loose cut-based photon ID. The Loose photon Id is applied as  
 965 in the EGamma POG recommandations for Run2 analyses [47] (tuned on Spring16 25 ns  
 966 samples). The isolation cuts (using the rho-area method for the mitigation of the pileup) and  
 967 conversion safe electron veto are applied. The isolation value is computed in a  $\Delta R$  cone of  
 968 0.3 and is corrected for pileup by subtracting the event-by-event energy density ( $\rho$ ) times an  
 969 effective area. The applied cut-based definition of the Loose photon Id is reported in Table 4.2.

Photons	Loose	
	EB	EE
$H/E$	<	0.0597
$\sigma_{i\eta i\eta}$	<	0.01031
PF ch.had.iso.( $\rho$ -corr)	<	1.295
PF neu.had.iso.( $\rho$ -corr)	<	$10.910 + 0.0148p_T + 0.000017p_T^2$
PF photon iso.( $\rho$ -corr)	<	$5.931 + 0.0163p_T + 0.000014p_T^2$
conversion veto		$3.630 + 0.0047p_T$
		$6.641 + 0.0034p_T$
	yes	yes

Table 4.2: Photon cut-based Id for Spring16 25ns conditions. EB: barrel cuts ( $|\eta_{\text{supercluster}}| \leq 1.479$ ); EE: endcap cuts ( $|\eta_{\text{supercluster}}| > 1.479$ )

970  
 971 Scale factors for photon identification (including isolation) are provided by Egamma POG,  
 972 derived for 80X (Moriond 17 recommendation), that can be found in [42].

## 4.2 Event selection

---

### 973 4.2.6 Jets

#### 974 How the jets are reconstructed

975 Events in the CMS detector are reconstructed using the particle-flow algorithm [48, 49],  
976 which combines information from all sub-detectors in order to reconstruct stable particles  
977 (muons, electrons, photons, neutral and charged hadrons). The charged hadron subtraction  
978 algorithm (CHS) removes candidates not associated to the primary vertex in order to remove  
979 contributions from pileup [50]. The remaining particles are used as input to jet clustering  
980 algorithms to reconstruct particle-flow jets. The jets are clustered using the FASTJET package [?]  
981 with the anti- $k_T$  jet clustering algorithm [51] with a clustering parameter of  $R = 0.8$  (“fat”-jets  
982 or AK8 jets) or  $R = 0.4$  (“standard”-jets or AK4 jets). In order to avoid double-counting of PF  
983 candidates, AK4 jets are considered only if the angular separation from the leading AK8 jet is  
984 larger than  $\Delta R > 0.8$ . Several levels of jet energy corrections are applied to the momentum of  
985 the clustered (raw) jets in order to obtain the energy value that is closer to the true energy of  
986 the initial parton [52]:

L1 Offset: the pileup and electronic noise effects are removed. This correction can be estimated  
988 using events collected by a random trigger, without any preconditions except a beam  
989 crossing, referred as zero bias events. The offset contribution from pileup is estimated by  
990 the FastJet method which relies on the definition of a jet area [?] from which a median  
991 energy density ( $\rho$ , in GeV/Area) per event can be defined. The correction subtracted  
992 to the jet  $p_T$  equals to  $\rho$  times the jet area. FastJet has the advantage of being able to  
993 remove the out-of-time pileup component, but has the disadvantage of subtracting the  
994 underlying event contribution as well.

L2 Relative ( $\eta$ ): the variation in jet response with  $\eta$  is flattened. The unbalance between the jets transverse  
996 momentum that is observed on average, is due to the variation of the jet response  
997 across the detector versus  $\eta$ .

L3 Absolute ( $p_T$ ): the calorimetric energy response varies as a function of the jet  $p_T$ . The absolute correction  
999 removes these variations and makes the response equal to unity. This correction is  
1000 obtained from simulation using the Monte Carlo truth information.

L2L3Residual: differences between data and simulation after L2 and L3 corrections are removed by  
1002 applying a specific calibration to data events. Residual corrections are extracted from  
1003 data using the transverse momentum balance in  $\gamma$ +jets and Z +jets events [52].

1004 The latest jet energy corrections are applied to AK4 and AK8 CHS jets, and the tags are  
1005 Summer16 23Sep2016V3.

1006 In this analysis, jets are considered if the corrected  $p_T$  is larger than 30 GeV for AK4  
1007 jets and 200GeV for AK8 jets, and lie in the tracker acceptance ( $|\eta| < 2.4$ ). Additionally,  
1008 AK4 are required to pass *loose* jet identification requirements, AK8 are required to pass *tight*  
1009 jet identification requirements defined by the JETMET POG for Run2 analyses [53], listed  
1010 in Table 4.3. AK8 jets are used to reconstruct the hadronically decaying electroweak boson  
1011 candidate, whilst AK4 jets are used to suppress the contribution of top and QCD background  
1012 events.

1013 Figure 4.2- 4.4 show the data/simulation comparison after the analysis selections (Tab. ??  
1014 without Top cleaning and Event cleaning).

PF Jet ID	<i>loose</i>	<i>tight</i>
Neutral Hadron Fraction	< 0.99	< 0.90
Neutral EM Fraction	< 0.99	< 0.90
Number of Constituents	> 1	> 1
Muon Fraction	-	-
Additionally, for $ \eta  < 2.4$		
Charged Hadron Fraction	> 0	> 0
Charged Multiplicity	> 0	> 0
Charged EM Fraction	< 0.99	< 0.99

Table 4.3: *Loose* and *Tight* jet identification requirements for Run2 (Spring16) 25ns conditions.

Figure 4.2: Number of reconstructed AK8 jets after selections.

Figure 4.3: Leading AK8 jet  $p_T$  spectra after selections.

Figure 4.4: Leading AK8 jet  $\eta$  spectra after selections.

1015 Since it has been measured that the jet energy resolution (JER) is not the same in data and  
 1016 MC, an additional smearing is applied in simulation, in order to get a better agreement, as  
 1017 suggested by JETMET POG [54].

There are two independent ways to get the smearing. With the scaling method, corrected four-momentum of a reconstructed jet is rescaled with a factor

$$c_{\text{JER}} = 1 + (s_{\text{JER}} - 1) \frac{p_T - p_T^{\text{ptcl}}}{p_T},$$

where  $p_T$  is its transverse momentum,  $p_T^{\text{ptcl}}$  is the transverse momentum of the corresponding jet clustered from generator-level particles, and  $s_{\text{JER}}$  is the data-to-simulation core resolution scale factor. Factor  $c_{\text{JER}}$  is truncated at zero, i.e. if it is negative, it is set to zero. This method only works if a well-matched particle-level jet is present and can result in a large shift of the response otherwise. The following requirements are imposed for the matching:

$$\Delta R < R_{\text{cone}}/2, |p_T - p_T^{\text{ptcl}}| < 3\sigma_{\text{JER}} p_T.$$

1018 Here  $R_{\text{cone}}$  is the jet cone size parameter (for instance, 0.4 for AK4 jets) and  $\sigma_{\text{JER}}$  is the relative  
 1019  $p_T$  resolution as measured in simulation.

An alternative approach, which does not require the presence of a matching particle-level jet, is the stochastic smearing. In this case corrected jet four-momentum is rescaled with a factor

$$c_{\text{JER}} = 1 + \mathcal{N}(0, \sigma_{\text{JER}}) \sqrt{\max(s_{\text{JER}}^2 - 1, 0)},$$

1020 where  $\sigma_{\text{JER}}$  and  $s_{\text{JER}}$  are the relative  $p_T$  resolution in simulation and data-to-simulation scale  
 1021 factors, and  $\mathcal{N}(0, \sigma)$  denotes a random number sampled from a normal distribution with a

## 4.2 Event selection

---

1022 zero mean and variance  $\sigma^2$ . As before, scaling factor  $c_{\text{JER}}$  is truncated at zero. This method  
1023 only allows to degrade the resolution.

1024 The smearing procedure adopted in this analysis is the hybrid method: when matching  
1025 particle-level jet is found, the scaling method is used; otherwise the stochastic smearing is  
1026 applied. The smearing coefficients and their errors, provided by JETMET POG, are reported  
1027 in Tab. 4.4 for 2016 data (tag: Spring1625nsV10).

Jet $\eta$	SF
0.0 – 0.5	$1.109 \pm 0.008$
0.5 – 0.8	$1.138 \pm 0.013$
0.8 – 1.1	$1.114 \pm 0.013$
1.1 – 1.3	$1.123 \pm 0.024$
1.3 – 1.7	$1.084 \pm 0.011$
1.7 – 1.9	$1.084 \pm 0.011$
1.9 – 2.1	$1.140 \pm 0.047$
2.1 – 2.3	$1.067 \pm 0.053$
2.3 – 2.5	$1.177 \pm 0.041$
2.5 – 2.8	$1.364 \pm 0.039$
2.8 – 3.0	$1.857 \pm 0.071$
3.0 – 3.2	$1.328 \pm 0.022$
3.2 – 5.0	$1.16 \pm 0.029$

Table 4.4: Smearing coefficients and JER uncertainties.

1028 **4.2.7 Jet mass**

1029 The jet mass is the main observable in distinguishing a V-jet from a QCD jet. Jet grooming  
 1030 consists in the suppression of uncorrelated UE/PU (underlying event and pile-up) radiation  
 1031 from the target jet and improves the discrimination pushing the jet mass for QCD jets towards  
 1032 lower values while maintaining the jet mass for V-jets around the boson-mass.

1033 The grooming algorithm considered in this analysis is the following:

**Soft-drop:** The “soft drop declustering” is a jet substructure technique which recursively removes soft wide-angle radiation from a jet [55]. The soft drop algorithm depends on two parameters: a soft threshold  $z_{cut}$  and an angular exponent  $\beta$ . Like any grooming method, soft drop declustering removes wide-angle soft radiation from a jet in order to mitigate the effects of contamination from initial state radiation (ISR), underlying event (UE), and multiple hadron scattering (pileup). Given a jet of radius  $R_0$  with only two constituents, the soft drop procedure removes the softer constituent unless:

$$\frac{\min(p_T^1, p_T^2)}{p_T^1 + p_T^2} > z_{cut} \left( \frac{\Delta R_{12}}{R_0} \right)^\beta$$

1034 By construction, this condition fail for wide-angle soft radiation. The degree of jet  
 1035 grooming is controlled by  $z_{cut}$  and  $\beta$ , with  $\beta \rightarrow \infty$  returning back an ungroomed jet.  
 1036 The  $\beta = 0$  limit of the energy loss is particularly interesting, since it is largely insensitive  
 1037 to the value of the strong coupling constant. The default parameters used by CMS are  
 1038  $\beta = 0$  and  $z_{cut} = 0.1$ .

1039 The grooming algorithm, **soft-drop**, is used in association with **PUPPI** in order to remove  
 1040 soft and wide-angle radiations and the pile-up contribution. It is a shared choice among all  
 1041 the diboson analyses, praised by theoreticians.

1042 Unfortunately, the default soft-drop + PUPPI jet mass suffers from a systematic shift from  
 1043 the expected value of about  $\sim 10\%$ , and some residual dependence on the jet  $p_T$ . Further  
 1044 corrections to the jet mass have been applied:

1045 **Gen:** a  $p_T$ -dependent correction to account for a small shift in the generated vector boson  
 1046 mass, applied only on simulated samples

1047 **Reco:** a  $p_T$ -dependent correction to the reconstructed jet mass, applied separately for jets in  
 1048 the barrel and endcaps regions

1049 These corrections are evaluated centrally by JMAR and documented in [56], and applied  
 1050 accordingly within the analysis.

1051 Figure 4.6- 4.7 show the jet mass for W or Z bosons before and after the correction, without  
 1052 applying any cut on this variable.

Figure 4.5: Softdrop + PUPPI mass of AK8 jet reconstructed for different bulk graviton signal samples; left: before corrections. right: after corrections.

1053 Furthermore, in order to obtain a better data-Monte Carlo agreement, a smearing proce-  
 1054 dure has been applied to the puppi softdrop mass, by using the stochastic method, with a  
 1055 constant smearing coefficient provided by JETMET POG ( $1.00 \pm 0.20$ ), that does not depend on  
 1056 jet pseudorapidity if it is restricted to  $|\eta| < 2.5$ .

## 4.2 Event selection

---

Figure 4.6: Softdrop + PUPPI mass of AK8 jet reconstructed for different  $W'$  signal samples; left: before corrections. right: after corrections.

Figure 4.7: Softdrop + PUPPI mass of AK8 jet; left: before corrections. right: after corrections.

1057 **4.2.8 Jet substructure**

In order to further discriminate signal from background, it is useful to investigate the inner structure of the jet. Studying the distribution of the jet constituents with respect to the jet axis allows us to test the hypothesis of the existence of multiple substructures, that could be evidence of jets originated by more than one parton. This procedure proceeds as follows: the constituents of the jet are clustered again with the  $k_T$  algorithm, however the procedure is stopped when one obtains N subjets. Then, a new variable, the N-subjettiness, is introduced. It is defined as:

$$\tau_N = \frac{1}{d_0} \sum_k p_{T,k} \min(\Delta R_{1,k}^\beta, \Delta R_{2,k}^\beta, \dots, \Delta R_{N,k}^\beta)$$

1058 where  $\beta$  is an arbitrary parameter, the index  $k$  runs over the jet constituents and the distances  
1059  $\Delta R_{N,k}$  are calculated with respect to the axis of the N-th subjet, obtained by one iteration of  $\tau$   
1060 minimization by varying the subjet axes around the  $k_T$  subjet axes.

The normalization factor  $d_0$  is calculated as  $d_0 = \sum_k p_{T,k} R_0^\beta$ , setting  $R_0$  to the radius of the original jet. The N-subjettiness is always included in the interval from 0 to 1 and represents the compatibility of the jet structure with an N-subjet hypothesis: small values correspond to high compatibility. Indeed,  $\tau_N$  weights the transverse momentum of the jet constituents by their angular distance to the closest subjet. In this analysis the N-subjettiness is calculated from the ungroomed jet with the parameter  $\beta = 1$ . The subjettiness related to the one and two subjet hypothesis is thus:

$$\tau_1 = \frac{1}{d_0} \sum_k p_{T,k} \Delta R_{1,k}$$

and

$$\tau_2 = \frac{1}{d_0} \sum_k p_{T,k} \min(\Delta R_{1,k}, \Delta R_{2,k})$$

1061 In principle, these two quantities should allow us to distinguish the dipole-like nature of the  
1062 showering of the Higgs decay from the classic monopole structure of QCD jets. In particular,  
1063 the variable that best discriminates between V-jets and QCD jets is the ratio of 2-subjettiness  
1064 and 1-subjettiness,  $\tau_{21} = \tau_2 / \tau_1$ .

1065 Figure 4.8 shows the  $\tau_{21}$  distributions for the PUPPI algorithm.

Figure 4.8:  $\tau_{21}$  subjettiness of PUPPI AK8 jet after inclusive selections.

---

### 1066 4.2.9 b-tagging

1067 B-tagging algorithms are applied to both the fat-jet and the sub-jets, independently. For sub-  
 1068 jets, run-II taggers are by default applied on the same charged particle-flow candidate list that  
 1069 is used in the jet clustering (*explicit jet-to-track association*). Thanks to the explicit jet-to-track  
 1070 association, the two sub-jets do not share any PF-constituent, avoiding unintended correla-  
 1071 tions.

1072 The jet or sub-jet is considered as tagged if the discriminator value is above some threshold  
 1073 value, often referred to as the cut value, and the efficiency is defined as the number of jets  
 1074 which have a discriminator value that is above that cut divided by the total number of jets (of  
 1075 the same flavor).

1076 The b-tagging algorithm used to set the analysis strategy is the Combined Secondary Ver-  
 1077 tex (CSV) [57] discriminator (full name `pfCombinedInclusiveSecondaryVertexV2BJetTags`).  
 1078 Different working points are provided by the POG for Run2 analyses [58], as shown in ta-  
 1079 ble 4.2.9, but the only one used in this analysis is the *loose* working point.

Working point	CSV cut	mis-tag probability
CSVL (Loose)	$> 0.5426$	$\approx 10\%$
CSVM (Medium)	$> 0.8484$	$\approx 1\%$
CSVT (Tight)	$> 0.9535$	$\approx 0.1\%$

Table 4.5: Working point for CSV b-tagging algorithm.

1080 B-tagging efficiency is not the same in data and MC. In order to take into account this dif-  
 1081 ference, the BTV POG provides collections of b-tagging scale factors for b-jets and mistagged  
 1082 light jets, measured for different physics processes, for the supported tagging algorithms and  
 1083 the three standard working points [57]. A weight is calculated on a per-event basis as a func-  
 1084 tion of the b-tagging status of the jets and their kinematic variables [59].

1085 In this analysis, b-tagging is used in order to reject events where a top quark is involved,  
 1086 by asking to the AK4 jets not laying in the AK8 jet cone to be anti b-tagged (in practice, the  
 1087 maximum CSV value allowed is the loose working point, CSVL).

### 1088 4.2.10 Missing Energy

#### 1089 How the MET is reconstructed

1090 The  $E_T^{\text{miss}}$  is the imbalance in the transverse momentum of all visible particles, and it is  
 1091 reconstructed with the particle flow algorithm [48]. The raw  $E_T^{\text{miss}}$  is defined as the inverse vec-  
 1092 torial sum of the transverse momentum of all the reconstructed charged and neutral particle  
 1093 flow candidates:  $E_T^{\text{miss}} = -\sum_{i=0}^{\text{all}} \vec{p}_{T,i}$ . The raw  $E_T^{\text{miss}}$  is systematically different from true  $E_T^{\text{miss}}$ ,  
 1094 for many reasons including the non-compensating nature of the calorimeters and detector  
 1095 misalignment. To better estimate the true  $E_T^{\text{miss}}$ , corrections can be applied:

1096 *Type-0*: a mitigation for the degradation of the  $E_T^{\text{miss}}$  reconstruction due to the pileup interac-  
 1097 tions, by applying the CHS algorithm. However, the  $E_T^{\text{miss}}$  contribution from pileup  
 1098 neutral particles cannot be easily subtracted; the assumption is that the  $E_T^{\text{miss}}$  contribu-  
 1099 tion term of charged and neutral pileup particles are the same, and cancellation at the  
 1100 true level is exact:  $\sum_{\text{neuPU}} \vec{p}_{T,i}^{\text{true}} + \sum_{\text{chPU}} \vec{p}_{T,i}^{\text{true}} = 0$ . An additional  $E_T^{\text{miss}}$  term is then  
 1101 added to the raw  $E_T^{\text{miss}}$  to take into account the neutral PU contribution, which is equal

## 4.2 Event selection

---

1102 to the charged one with a multiplicative scale factor taking into account calorimeter  
1103 mismeasurements of low- $p_T$  energy deposits.

1104 Type-1: propagation of the jet energy corrections (JEC) to MET. The Type-I correction replaces  
1105 the vector sum of transverse momenta of particles which can be clustered as jets with  
1106 the vector sum of the transverse momenta of the jets to which JEC is applied.

1107 Particle flow  $E_T^{\text{miss}}$  with type-1 corrections applied is currently the default one used by CMS  
1108 physics analyses. Additionally, some  $E_T^{\text{miss}}$  filters have been recommended by JETMET POG  
1109 for Run2 analyses [53], in order to remove events with spurious  $E_T^{\text{miss}}$  related to detector noise  
1110 and bad reconstructions, and they are listed in sec. ??.

1111 Since the  $E_T^{\text{miss}}$  corrections and uncertainties depend on the JEC applied, they are re-  
1112 computed accordingly following the JETMETPOG recommendation:

```
1113 from PhysicsTools.PatUtils.tools.runMETCorrectionsAndUncertainties import
1114 runMetCorAndUncFromMiniAOD
1115 # If you only want to re-correct and get the proper uncertainties
1116 runMetCorAndUncFromMiniAOD(process,
1117                         isData=True (or False),
1118                         )
1119 process.p = cms.Path(process.fullPatMetSequence *
1120     process.yourAnalyzer)
1121
1122 cms.InputTag("slimmedMETS", "", "YourProcessName")
```

1123 Figure 4.9 show the  $E_T^{\text{miss}}$  distribution for data and Monte Carlo after the corrections and  
1124 filters.

Figure 4.9: Type-1 corrected  $E_T^{\text{miss}}$  distribution after inclusive selections.

<sub>1125</sub> **4.3 Diboson candidate reconstruction**

#### **4.4 Background estimation**

---

<sub>1126</sub> **4.4 Background estimation**

<sub>1127</sub> **4.5 Systematic uncertainties**

## **4.6 Results**

---

1128 **4.6 Results**



# Combination of diboson searches in semileptonic final states



---

---

1132

Chapter

6

## Conclusions

1133

1134



1135

## Bibliography

1136

1137

- 1138 [1] G. Aad *et al.*, "Observation of a new particle in the search for the Standard Model Higgs  
1139 boson with the ATLAS detector at the LHC," *Phys. Lett. B*, vol. 716, p. 1, 2012.
- 1140 [2] S. Chatrchyan *et al.*, "Observation of a new boson at a mass of 125 GeV with the CMS  
1141 experiment at the LHC," *Phys. Lett. B*, vol. 716, p. 30, 2012.
- 1142 [3] S. Chatrchyan *et al.*, "Observation of a new boson with mass near 125 GeV in pp collisions  
1143 at  $\sqrt{s} = 7$  and 8 TeV," *JHEP*, vol. 06, p. 081, 2013.
- 1144 [4] G. Aad *et al.*, "Evidence for the spin-0 nature of the Higgs boson using ATLAS data,"  
1145 *Phys. Lett. B*, vol. 726, p. 120, 2013.
- 1146 [5] V. Khachatryan *et al.*, "Precise determination of the mass of the Higgs boson and tests of  
1147 compatibility of its couplings with the standard model predictions using proton collisions  
1148 at 7 and 8 TeV," *Eur. Phys. J. C*, vol. 75, p. 212, 2015.
- 1149 [6] G. Aad *et al.*, "Measurement of the Higgs boson mass from the  $H \rightarrow \gamma\gamma$  and  $H \rightarrow ZZ^* \rightarrow$   
1150  $4\ell$  channels in  $pp$  collisions at center-of-mass energies of 7 and 8 TeV with the ATLAS  
1151 detector," *Phys. Rev. D*, vol. 90, p. 052004, 2014.
- 1152 [7] CMS and ATLAS Collaborations, "Combined Measurement of the Higgs Boson Mass in  
1153  $pp$  Collisions at  $\sqrt{s} = 7$  and 8 TeV with the ATLAS and CMS Experiments." Submitted  
1154 to *Phys. Rev. Lett.*, 2015.
- 1155 [8] G. Degrassi, S. Di Vita, J. Elias-Miro, J. R. Espinosa, G. F. Giudice, G. Isidori, and A. Stru-  
1156 mua, "Higgs mass and vacuum stability in the Standard Model at NNLO," *JHEP*, vol. 08,  
1157 p. 098, 2012.
- 1158 [9] D. Pappadopulo, A. Thamm, R. Torre, and A. Wulzer, "Heavy vector triplets: bridging  
1159 theory and data," *Journal of High Energy Physics*, vol. 2014, no. 9, pp. 1–50, 2014.
- 1160 [10] V. D. Barger, W.-Y. Keung, and E. Ma, "A Gauge Model With Light W and Z Bosons,"  
1161 *Phys. Rev.*, vol. D22, p. 727, 1980.

- 1162 [11] C. Grojean, E. Salvioni, and R. Torre, "A weakly constrained W' at the early LHC," *JHEP*,  
1163 vol. 07, p. 002, 2011.
- 1164 [12] R. Contino, D. Pappadopulo, D. Marzocca, and R. Rattazzi, "On the effect of resonances  
1165 in composite higgs phenomenology," *Journal of High Energy Physics*, vol. 2011, no. 10,  
1166 pp. 1–50, 2011.
- 1167 [13] B. Bellazzini, C. Csáki, and J. Serra, "Composite Higgses," *Eur. Phys. J.*, vol. C74, no. 5,  
1168 p. 2766, 2014.
- 1169 [14] G. F. Giudice, C. Grojean, A. Pomarol, and R. Rattazzi, "The Strongly-Interacting Light  
1170 Higgs," *JHEP*, vol. 06, p. 045, 2007.
- 1171 [15] A. Wulzer, "An Equivalent Gauge and the Equivalence Theorem," *Nucl. Phys.*, vol. B885,  
1172 pp. 97–126, 2014.
- 1173 [16] A. M. Sirunyan *et al.*, "Search for massive resonances decaying into WW, WZ, ZZ, qW,  
1174 and qZ with dijet final states at  $\sqrt{s} = 13$  TeV," 2017.
- 1175 [17] CMS Collaboration, "Search for massive resonances decaying into WW, WZ, ZZ, qW and  
1176 qZ in the dijet final state at  $\sqrt{s} = 13$  TeV," CMS Physics Analysis Summary CMS-PAS-  
1177 B2G-17-001, CERN, Geneva, 2017.
- 1178 [18] C. Collaboration, "Search for heavy resonances decaying into a vector boson and a Higgs  
1179 boson in hadronic final states with 2016 data," 2017.
- 1180 [19] CMS Collaboration, "Search for heavy resonances decaying into a vector boson and a  
1181 Higgs boson in hadronic final states with 2016 data," CMS Physics Analysis Summary  
1182 CMS-PAS-B2G-17-002, CERN, Geneva, 2017.
- 1183 [20] CMS Collaboration, "Search for heavy resonances decaying into a Z boson and a W  
1184 boson in the  $\ell^+\ell^-q\bar{q}$  final state," CMS Physics Analysis Summary CMS-PAS-B2G-16-022,  
1185 CERN, Geneva, 2017.
- 1186 [21] V. Khachatryan *et al.*, "Search for heavy resonances decaying into a vector boson and a  
1187 Higgs boson in final states with charged leptons, neutrinos, and b quarks," *Phys. Lett.*,  
1188 vol. B768, pp. 137–162, 2017.
- 1189 [22] CMS Collaboration, "Search for new resonances decaying to  $WW/WZ \rightarrow \ell\nu qq$ ," CMS  
1190 Physics Analysis Summary CMS-PAS-B2G-16-020, CERN, Geneva, 2016.
- 1191 [23] CMS Collaboration, "Search for heavy resonances decaying into a Z boson and a vector  
1192 boson in the  $\nu\nu q\bar{q}$  final state," CMS Physics Analysis Summary CMS-PAS-B2G-17-005,  
1193 CERN, Geneva, 2017.
- 1194 [24] M. Aaboud *et al.*, "Search for diboson resonances with boson-tagged jets in  $pp$  collisions  
1195 at  $\sqrt{s} = 13$  TeV with the ATLAS detector," 2017.
- 1196 [25] ATLAS Collaboration, "Search for  $WW/WZ$  resonance production in  $\ell\nu qq$  final states in  
1197  $pp$  collisions at  $\sqrt{s} = 13$  TeV with the ATLAS detector," ATLAS Conference Note ATLAS-  
1198 CONF-2017-051, CERN, Geneva, Jul 2017.

## BIBLIOGRAPHY

---

- 1199 [26] “Searches for heavy ZZ and ZW resonances in the llqq and vvqq final states in pp collisions at  $\text{sqrt}(s) = 13 \text{ TeV}$  with the ATLAS detector,” ATLAS Conference Note ATLAS-  
1200 CONF-2016-082, CERN, Geneva, Aug 2016.  
1201
- 1202 [27] M. Aaboud *et al.*, “Search for heavy resonances decaying to a W or Z boson and a Higgs  
1203 boson in the  $q\bar{q}^{(\prime)} b\bar{b}$  final state in  $pp$  collisions at  $\sqrt{s} = 13 \text{ TeV}$  with the ATLAS detector,”  
1204 2017.
- 1205 [28] ATLAS Collaboration, “Search for heavy resonances decaying to a W or Z boson and a Higgs  
1206 boson in final states with leptons and  $b$ -jets in  $36.1 \text{ fb}^{-1}$  of  $pp$  collision data at  
1207  $\sqrt{s} = 13 \text{ TeV}$  with the ATLAS detector,” ATLAS Conference Note ATLAS-CONF-2017-  
1208 055, CERN, Geneva, Jul 2017.
- 1209 [29] L. Randall and R. Sundrum, “A Large mass hierarchy from a small extra dimension,”  
1210 *Phys. Rev. Lett.*, vol. 83, pp. 3370–3373, 1999.
- 1211 [30] L. Randall and R. Sundrum, “An Alternative to compactification,” *Phys. Rev. Lett.*, vol. 83,  
1212 pp. 4690–4693, 1999.
- 1213 [31] K. Agashe, H. Davoudiasl, G. Perez, and A. Soni, “Warped Gravitons at the LHC and  
1214 Beyond,” *Phys. Rev.*, vol. D76, p. 036006, 2007.
- 1215 [32] A. L. Fitzpatrick, J. Kaplan, L. Randall, and L.-T. Wang, “Searching for the Kaluza-Klein  
1216 Graviton in Bulk RS Models,” *JHEP*, vol. 09, p. 013, 2007.
- 1217 [33] H. Davoudiasl, J. L. Hewett, and T. G. Rizzo, “Phenomenology of the Randall-Sundrum  
1218 Gauge Hierarchy Model,” *Phys. Rev. Lett.*, vol. 84, p. 2080, 2000.
- 1219 [34] T. Gherghetta and A. Pomarol, “Bulk fields and supersymmetry in a slice of AdS,” *Nucl.*  
1220 *Phys.*, vol. B586, pp. 141–162, 2000.
- 1221 [35] H. Davoudiasl, J. L. Hewett, and T. G. Rizzo, “Experimental probes of localized gravity:  
1222 On and off the wall,” *Phys. Rev.*, vol. D63, p. 075004, 2001.
- 1223 [36] A. Oliveira, “Gravity particles from Warped Extra Dimensions, predictions for LHC,”  
1224 2014.
- 1225 [37] CMS Collaboration, “Search for diboson resonances in the  $2l2\nu$  final state,” CMS Physics  
1226 Analysis Summary CMS-PAS-B2G-16-023, CERN, Geneva, 2017.
- 1227 [38] CMS Collaboration, “Search for heavy resonances decaying to a pair of Higgs bosons in  
1228 the four b quark final state in proton-proton collisions at  $\sqrt{s} = 13 \text{ TeV}$ ,” CMS Physics  
1229 Analysis Summary CMS-PAS-B2G-16-026, CERN, Geneva, 2017.
- 1230 [39] “Pileup Reweighting Procedure - <https://twiki.cern.ch/twiki/bin/viewauth/CMS/PileupReweighting>,”  
1231
- 1232 [40] “Utilities for Accessing Pileup Information for Data - <https://twiki.cern.ch/twiki/bin/view/CMS/PileupJSONFileforData>,”  
1233
- 1234 [41] “EGamma POG - Cut based electron ID for Run2 - <https://twiki.cern.ch/twiki/bin/view/CMS/CutBasedElectronIdentificationRun2>,”  
1235

- 1236 [42] “EGamma POG - Electron ID recipes for Run2 - <https://twiki.cern.ch/twiki/bin/view/CMS/EgammaIDRecipesRun2>,”
- 1237
- 1238 [43] CMS Collaboration, “Performance of cms muon reconstruction in pp collision events at  
1239  $\sqrt{s} = 7\text{TeV}$ .” Submitted to *J. Inst.*, 2012.
- 1240 [44] R. Fruhwirth, “Application of kalman filtering to track and vertex fitting,” *Nuclear Instruments and Methods in Physics Research Section A: Accelerators, Spectrometers, Detectors and Associated Equipment*, vol. 262, no. 23, pp. 444 – 450, 1987.
- 1241
- 1242
- 1243 [45] “Reference muon id, isolation and trigger efficiencies for Run-II -  
1244 <https://twiki.cern.ch/twiki/bin/view/CMS/MuonReferenceEffsRun2>,”
- 1245 [46] “Tau POG - Tau ID for Run2 - <https://twiki.cern.ch/twiki/bin/viewauth/CMS/-TauIDRecommendation13TeV>,”
- 1246
- 1247 [47] “EGamma POG - Cut based photon ID for Run2 - <https://twiki.cern.ch/twiki/bin/view/CMS/CutBasedPhotonIdentificationRun2>,”
- 1248
- 1249 [48] CMS Collaboration, “Particle-flow event reconstruction in CMS and performance for jets,  
1250 taus, and  $E_T^{\text{miss}}$ ,” no. CMS-PAS-PFT-09-001, 2009.
- 1251 [49] CMS Collaboration, “Commissioning of the particle-flow event reconstruction with the  
1252 first LHC collisions recorded in the CMS detector,” no. CMS-PAS-PFT-10-001, 2010.
- 1253 [50] “Pileup Removal Algorithms,” Tech. Rep. CMS-PAS-JME-14-001, CERN, Geneva, 2014.
- 1254 [51] M. Cacciari, G. P. Salam, and G. Soyez, “The anti- $k_t$  jet clustering algorithm,” *JHEP*,  
1255 vol. 04, p. 063, 2008.
- 1256 [52] T. C. collaboration, “Determination of jet energy calibration and transverse momentum  
1257 resolution in cms,” *Journal of Instrumentation*, vol. 6, no. 11, p. P11002, 2011.
- 1258 [53] “JetMET POG - Jet ID for Run2 - <https://twiki.cern.ch/twiki/bin/view/CMS/JetID>,”
- 1259 [54] “Jetmet pog - jet energy resolution smearing - <https://twiki.cern.ch/twiki/bin/view/cms/jetresolution>,”
- 1260
- 1261 [55] A. J. Larkoski, S. Marzani, G. Soyez, and J. Thaler, “Soft Drop,” *JHEP*, vol. 05, p. 146,  
1262 2014.
- 1263 [56] T. K. Arrestad et al., “Identification and calibration of boosted hadronic W/Z bosons at  
1264 13 TeV,” tech. rep., AN-2016/215, 2016.
- 1265 [57] S. Chatrchyan et al., “Identification of b-quark jets with the CMS experiment,” *JINST*,  
1266 vol. 8, p. P04013, 2013.
- 1267 [58] “BTV POG - B-tagging for Run2 - <https://twiki.cern.ch/twiki/bin/view/CMS/BtagRecommendation80X>,”
- 1268
- 1269 [59] “Methods to apply b-tagging efficiency scale factors,” 2013.